

AD-A111 349

NAVAL RESEARCH LAB WASHINGTON DC

F/6 20/7

DYNAMICS OF A ROTATING PROTON LAYER ALONG A MAGNETIC RAMP. (U)

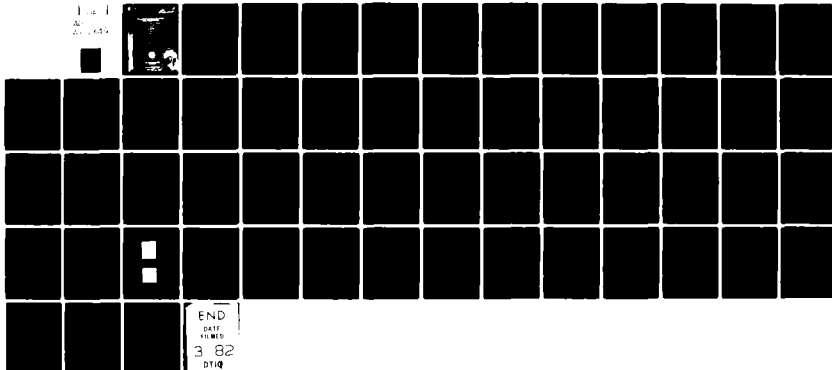
DEC 81 J GOLDEN, J A PASOUR, C A KAPETANAKOS EX-77-A-34-1013

UNCLASSIFIED

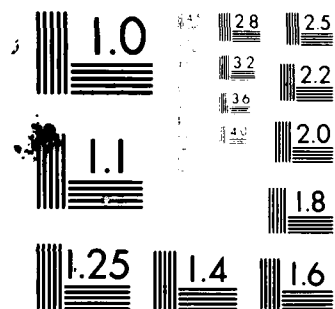
NRL-MR-4699

NL

1.1  
2.1



END  
DATE  
FILMED  
3 82  
DTIC



MICROCOPY RESOLUTION TEST CHART  
 NATIONAL BUREAU OF STANDARDS-1963-A



SECURITY CLASSIFICATION OF THIS PAGE (When Data Entered)

REPORT DOCUMENTATION PAGE		READ INSTRUCTIONS BEFORE COMPLETING FORM
1. REPORT NUMBER NRL Memorandum Report 4699	2. GOVT ACCESSION NO. AD-A-111-111	3. RECIPIENT'S CATALOG NUMBER 111-111
4. TITLE (and Subtitle) DYNAMICS OF A ROTATING PROTON LAYER ALONG A MAGNETIC RAMP		5. TYPE OF REPORT & PERIOD COVERED Final report on an NRL problem
		6. PERFORMING ORG. REPORT NUMBER
7. AUTHOR(s) J. Golden, S. J. Marsh*, J. A. Pasour, D. Pershing†, and C. A. Kapetanakis		8. CONTRACT OR GRANT NUMBER(s)
9. PERFORMING ORGANIZATION NAME AND ADDRESS Naval Research Laboratory Washington, D.C. 20375		10. PROGRAM ELEMENT, PROJECT, TASK AREA & WORK UNIT NUMBERS 61153N;RR0110941;47-0869-0-0 DOE/EX77-A-34-1013;47-0872-0-0
11. CONTROLLING OFFICE NAME AND ADDRESS		12. REPORT DATE December 31, 1981
		13. NUMBER OF PAGES 56
14. MONITORING AGENCY NAME & ADDRESS (if different from Controlling Office)		15. SECURITY CLASS. (of this report) UNCLASSIFIED
		15a. DECLASSIFICATION/DOWNGRADING SCHEDULE
16. DISTRIBUTION STATEMENT (of this Report)  Approved for public release; distribution unlimited.		
17. DISTRIBUTION STATEMENT (of the abstract entered in Block 20, if different from Report)		
18. SUPPLEMENTARY NOTES  *Sachs-Freeman Associates, Bowie, MD 20715 †Jaycor, Inc., Alexandria, VA. Work performed in part as an NRC Research Associate.		
19. KEY WORDS (Continue on reverse side if necessary and identify by block number)  Field-reversed ion rings Ion beam applications Controlled thermonuclear fusion Applications of pulsed power		
20. ABSTRACT (Continue on reverse side if necessary and identify by block number)  The dynamics of a rotating proton layer containing $2 - 6 \times 10^{16}$ protons of 1 - 1.5 MeV energy propagating in vacuum along a ramp magnetic field have been studied experimentally and by computer simulation. The layer is produced by passing the annular proton pulse produced by an Inverse Reflex Tetrode (IRT) through a magnetic cusp. The diamagnetic self-magnetic field (as high as 1.6 times the applied field) and the radial oscillations of the layer are monitored. The axial velocity of the pulse is determined, and a maximum of 1.7 is obtained for the ratio of azimuthal to axial velocity. The layer (continued)		

DD FORM 1473  
1 JAN 73

EDITION OF 1 NOV 65 IS OBSOLETE  
S/N 0102-014-6601

SECURITY CLASSIFICATION OF THIS PAGE (When Data Entered)

20 ABSTRACT (Continued)

has also been propagated along the ramp in the presence of a neutral gas cloud with pressure  $\geq 0.1$  Torr. Computer simulation of the experiment uses an axisymmetric particle-in-cell code that includes self- and external-  $B_z$  and  $B_r$  magnetic fields and the inductive  $E_\theta$  electric field. Calculated contour maps of the particle and current densities of the beam at selected times are presented. The computer particle density profile, the ratio  $v_\theta/v_z$ , and the magnitude of the diamagnetic signals are in qualitative agreement with the observations.

*1*

*4-6-61*

## CONTENTS

I. INTRODUCTION .....	1
II. DESCRIPTION OF THE EXPERIMENTAL APPARATUS .....	3
III. PROPAGATION OF THE ROTATING PROTON PULSE .....	7
IV. INTERACTION WITH NEUTRAL GAS .....	17
V. SUMMARY .....	19
REFERENCES .....	20



# DYNAMICS OF A ROTATING PROTON LAYER ALONG A MAGNETIC RAMP

## I. INTRODUCTION

Reversed-field magnetic configurations with closed field lines generated by energetic particles have potential application in controlled thermonuclear fusion<sup>1-9</sup> and in novel particle acceleration<sup>10-11</sup> schemes. With respect to controlled thermonuclear fusion, such magnetic configurations appear attractive because the closed field lines may considerably enhance the confinement time of a fusion plasma and the gyrating particles can serve as an internal source of energy for heating the confined plasma.

Initially, the research effort was focused on the formation of relativistic electron layers.<sup>12,13</sup> However, field reversal generated by relativistic electrons is not of interest for thermonuclear applications because of synchrotron radiation losses. To avoid the radiation losses, Christofilos<sup>14</sup> proposed the use of ions with GeV energy instead of electrons. In the Christofilos scheme, as well as a similar scheme proposed by McNally,<sup>15</sup> the ion beams are generated by conventional accelerators and have very low current ( $\sim 1$  mA). Therefore, the use of conventional, low current accelerators leads to long buildup times and requires extremely low particle loss rates.

However, high current ion sources that have been developed recently make possible the formation of field reversed ion rings in very short times. The first experiments to produce proton layers by injection into a cusp used proton beams generated by reflex triodes<sup>16</sup> and magnetically insulated diodes.<sup>17</sup> These beams contained only  $10^{14} - 10^{15}$  protons and produced diamagnetic self fields that were  $\leq 3\%$  of the applied field. With improvements in reflexing-electron ion sources<sup>18,19</sup> and magnetically insulated diodes,<sup>20,21</sup> beams containing  $10^{16} - 10^{17}$  protons per pulse have become available. These advances in beam generation made possible the transient field reversal by a rotating proton layer.<sup>22</sup>

Because the number of protons available in a pulse is comparable to the number required for field reversal, the formation and trapping of the rotating layer must be accomplished with small particle losses. In addition, the axial velocity of the proton pulse must be reduced almost to zero to achieve trapping of the protons within the potential well of a magnetic mirror. The required axial slowing can result from inductive coupling of the beam self-magnetic field to a resistive medium<sup>23</sup> or by propagation of the layer along an increasing magnetic field, i.e., a magnetic ramp. This paper reports on the propagation of a field-reversed rotating proton layer along a magnetic ramp and compares the experimental observations with computer simulations. In the experiment, the propagation is studied both in vacuum and in the presence of a neutral gas cloud injected into the path of the beam.

Experiments have been performed in which an annular beam containing  $2-6 \times 10^{16}$  protons of energy  $\sim 1-1.5$  MeV passes through a magnetic cusp and propagates along a magnetic ramp. Measurements indicate that the diamagnetic axial self field of the proton layer is as high as 1.6 times the applied magnetic field. However the amplitude of the diamagnetic signal depends strongly on the strength of the applied magnetic field and on the self fields in the Inverse Reflex Tetrode (IRT) ion source.<sup>24,25</sup> Similarly it is found that the loss of protons to the wall and the radial distribution within the rotating layer are predominantly influenced by the self fields in the source and in the cusp. Because of the strong self fields, the particle dynamics are considerably different from those of single particles in the absence of significant self fields. For this reason, the axial velocity of the rotating layer is higher than expected for the single particle case.

To better understand the effects of the self fields, the experiment was simulated by a particle-in-cell computer code. In this code the electron dynamics were omitted. The effects of self electric and magnetic fields in the IRT were taken into account by specifying the transverse and axial velocity components as a function of radius at the cathode plane, i.e., as initial conditions prior to injection into the cusp field. Although greatly simplified, this model permitted the study of the dynamics of the layer in the cusp and in the ramp fields. The simulation successfully predicted most of the experimental observations, for example, the number and location of the losses at the wall, the radial distribution, time-of-flight, and qualitatively, the behavior of the diamagnetic signal.

Experiments were also performed with a neutral gas cloud in the ramp. This gas cloud, air or  $N_2$ , was injected by fast puff valves. It was found that the beam ionized the gas and induced azimuthal plasma currents which magnetically neutralized the layer. In contrast to experiments<sup>23</sup> at Cornell University, only a modest axial slowing of the layer was observed. This is attributed to the small ratio of the azimuthal velocity  $v_\theta$  to the axial velocity  $v_z$ , i.e.,  $v_\theta/v_z < 1$ . The time behavior of the diamagnetic signal after the passage of the layer can be explained by the excitation of magnetosonic waves. In addition, several features of the diamagnetic signals of the Cornell experiment can also be explained by this hypothesis.

In the most recent experiments it has been shown that by increasing the radius of the beam at injection and suitably shaping the electrodes of the IRT source, rotating layers not strongly perturbed by self fields and having  $v_\theta/v_z \sim 1.7$  can be produced. Such layers appear to be suitable for subsequent trapping in a magnetic mirror with a time dependent gate field.

In this paper, Section II is a description of the experimental apparatus, the magnetic configurations used, and a summary of the diagnostic methods. The experimental observations of the propagation of the rotating pulse are presented and compared with the computer simulation results in Section III. The interaction of the layer with neutral gas is discussed in Section IV. A summary discussion of the results is given in Section V.

## II. DESCRIPTION OF THE EXPERIMENTAL APPARATUS

A schematic of the experiment is shown in Fig. 1. The IRT is powered by the upgraded Gamble II generator. This apparatus is the same one used in the previously reported experiment on the transient field reversal by a rotating proton layer.<sup>22</sup> However in the previous experiment, the magnetic field configuration consisted of a magnetic cusp followed by a 75 cm long uniform field and a single magnetic mirror. In the present experiment, the magnetic configuration is comprised of a 60-cm-transition-width magnetic cusp followed by an increasing magnetic ramp. The pulsed electromagnets that produce this applied field are multiple-tapped coils that can produce several field shapes. Some of the magnetic field

configurations used are shown in Fig. 2. In this figure the axial magnetic field at a radius of 10 cm is plotted as a function of axial position. The  $\delta$  configuration is most often used. The  $\kappa$  configuration is a shorter system that has the same field shape as the  $\delta$  configuration so that a higher field can be obtained for a given energy stored in the capacitor bank. The  $\eta$  configuration produces a higher mirror peak than the  $\delta$  configuration. The  $\lambda$  configuration gives a higher gradient. In the previously reported experiments, the  $\beta$  configuration was used.

The electromagnets are energized by a capacitor bank with a nominal energy store of  $\sim 1$  MJ. The field rise time is typically 5-10 ms and is long enough to penetrate the 3 mm thick stainless steel walls of the vacuum chamber.

The inverse reflex tetrode source consists of a stainless steel screen cathode K (75% open area) and an annular polyethylene anode A of typically 18.5 cm i.d., 37 cm o.d., and 100  $\mu$ m thickness mounted on a 37 cm o.d., cylindrical anode stalk. At the end of the stalk opposite the anode is a 3 mm thick stainless steel plate. Electrically connected to the plate is a movable stainless steel disc G located 23 cm from A. Electrons emitted from the grounded cathode K are accelerated toward the semitransparent anode, pass through it and form a virtual cathode VC between A and G. Those electrons transmitted through the VC reach the grid. The rest of the electrons reflex between VC and K until they are absorbed. The protons are extracted out of the plasma that is formed from the plastic anode. When the applied voltage increases or remains constant, protons directed toward VC are unable to reach G or they reach it with zero velocity. Some of these backward directed protons are reflected and after passing through the hole at the center of the anode are accelerated and join the remainder of the beam. Typically the operating pressure in the system is below 0.7 mTorr.

For the present set of experiments, the IRT has been modified so that conical anode and cathode electrodes can be used (see Fig. 1). These electrodes provide a radial component to the applied electric field. This radial field can reduce or increase the inward radial component of velocity that the protons acquire in crossing the A-K gap. Thus, the pinching effect of the azimuthal self-magnetic field  $B_\theta$  and

radial self-electric field  $E_r^{\text{self}}$  (that is caused by excessive negative charge near the axis within the gap) can be substantially controlled for most of the pulse.

It is desirable that the performance of the IRT not depend strongly on the applied axial magnetic field  $B_0$  (in the A-K gap). This has been achieved by suitably choosing the thickness of the anode plastic and the correct A-K gap for a particular  $B_0$  and applied potential. As described previously,<sup>19</sup> for a proper choice of applied voltage, anode thickness, and applied magnetic field, the IRT operates with a nearly constant impedance  $Z$  during an appreciable fraction of the 80 nsec (FWHM) long pulse. Typical waveforms of the voltage across the A-K gap (equal to the applied potential minus the  $LI$  inductive contribution) and the total current are shown in Fig. 3. The voltage initially rises to  $\sim 0.5$  MV in 10-15 nsec and then increases to  $\sim 1.5$  MV within 60 nsec. The peak total current is  $\sim 0.9$  MA, and the peak power of the device is  $\sim 1.4$  TW. The peak proton current is 250 kA, and typical proton pulses have a time-averaged proton current  $\bar{I}_p$  of 65-110 kA; the time averaged total current  $\bar{I}_0$  is  $\sim 0.4$ -0.5 MA. The proton generation efficiency defined as the ratio  $\bar{I}_p/\bar{I}_0$  is between 15 percent and 25 percent. The ion generation efficiency may be much higher because ions other than protons are not monitored.

The principal methods for diagnosing the beam parameters are nuclear activation analysis,<sup>26</sup> prompt  $\gamma$ -ray measurements,<sup>27</sup> magnetic loops, and witness plates. The number of protons  $N_p$  at various radial and axial positions is inferred from measurement of the residual radioactivity induced in carbon targets via the resonant nuclear reaction  $^{12}\text{C} (p, \gamma) ^{13}\text{N} (\beta^+) ^{13}\text{C}$ . The number of delayed  $\gamma$ -rays emitted from the annihilation of the positrons is corrected for contributions from the reaction  $^{12}\text{C} (d, n) ^{13}\text{N} (\beta^+) ^{13}\text{C}$  induced by the natural isotopic abundance of deuterium in polyethylene. No correction is made for blowoff, i.e., the loss of  $^{13}\text{N}$  nuclei prior to detection. The radial profile of the beam is determined by individually counting small segments of a carbon target activated by the beam. Similarly, the loss of protons to the wall is determined from arrays of activation targets located at the wall, and loss to the on-axis probe assembly is determined from carbon cloth targets wrapped around the shaft supporting the probe.

Time-of-flight  $\Delta t$  of the rotating layer is obtained from the delay between the voltage pulse and the emission of prompt  $\gamma$ -rays when the protons strike a teflon target and induce the nuclear reaction  $^{19}\text{F}(p, \alpha\gamma)^{16}\text{O}$ . The prompt  $\gamma$  rays are detected by an NPM-54 photomultiplier and fast scintillator located inside a lead housing having a wall thickness in excess of 5 cm.

The shape of the prompt  $\gamma$ -ray pulse also provides information about the duration and time dependence of the proton pulse. However, because of the sensitive dependence of the thick target yield of the nuclear reaction on the energy distribution of the protons,<sup>27</sup> only approximate information about the time dependence of the proton flux can be inferred.

The on-axis diamagnetic signals  $\delta B_z$  are monitored with 3 pickup-loops spaced 50 cm apart and mounted in a common probe housing made of glass. The pickup-loops consist of 6 turns and are center tapped. The wires are brought out through a thin-walled stainless steel tube within the 1.5 cm o.d. glass housing. A passive mixer or the mixer in the vertical amplifier of the oscilloscope is used to subtract the signals from the two halves of each pickup coil so that the electrostatic components of the signals cancel but the magnetic components are added. The signals are passively RC integrated. Typical sensitivity is  $\sim 30$  Gauss per volt in a 50 ohm impedance load with an integration time constant  $RC \sim 2 \mu\text{sec}$ . The probes are calibrated using a test fixture which precisely positions the probe within a Helmholtz coil. In addition to the on-axis probes, several probes are located at various axial positions at the chamber wall. These wall probes can be positioned to measure either the  $\delta B_z$  or the azimuthal self magnetic field  $\delta B_\theta$ .

Additional information about the spatial location of the proton layer is obtained using "witness targets" of brass or plastic. X-rays from electron Bremsstrahlung in the IRT are monitored with a scintillator and photodiode.

### III. PROPAGATION OF THE ROTATING PROTON PULSE

#### (a) Experiment

A series of experiments was performed to determine the main features of the propagation of the rotating beam along the magnetic ramp. The objectives of these experiments were to measure the ratio  $v_\theta/v_z$ , the loss of protons to the chamber wall, the strength of the diamagnetic signal  $\delta B_z$  and the radial profile of the beam at several axial positions along the ramp.

The amplitude and axial variation of  $\delta B_z$  depend sensitively on the injection angle  $\phi$  which may be defined as  $\tan^{-1} v_r/v_z$ , where  $v_r$  and  $v_z$  are the mean values of the radial and axial components of velocity at the cathode. This is demonstrated by varying the electrode angle  $\theta_{IRT}$ , (see Fig. 1) which changes  $\phi$ . A comparison of the  $\delta B_z$  signals for  $\theta_{IRT} = 0^\circ$  (shot 381) and  $\theta_{IRT} = 9^\circ$  (shot 475) can be made from the data given in Table 1. Tabulated for several representative shots are the on-axis  $\delta B_z$  signals ( $\delta B_{z1}$ ,  $\delta B_{z2}$  and  $\delta B_{z3}$ ) monitored by the 3-probe assembly. The probes are spaced 50 cm apart and the  $\delta B_{z1}$  probe is located 45 cm from the cusp for shot 381 and 50 cm from the cusp for the other shots listed in the table. The comparison shows that the  $\delta B_z$  signals are an order of magnitude smaller for the  $\theta_{IRT} = 9^\circ$  than  $\theta_{IRT} = 0^\circ$ . Also evident is the drop in  $\delta B_z$  that occurs as the beam propagates further downstream. The corresponding field reversal factor  $\zeta = (\delta B_{z1}/B_{z1}, \delta B_{z2}/B_{z2}, \delta B_{z3}/B_{z3})$  where  $B_{zn}$  is the applied field at the position of the  $n$ th probe, also decreases along the ramp. For the  $\theta_{IRT} = 0^\circ$  case,  $\zeta = (1.25, 0.25, 0.06)$ ; for the  $\theta_{IRT} = 9^\circ$  case,  $\zeta = (0.09, 0.015, 0.005)$ .

The difference in the strength of  $\delta B_z$  for the two values of  $\theta_{IRT}$  can be explained by a difference in the injection angle  $\phi$  and subsequent radial oscillation. For the  $\theta_{IRT} = 0^\circ$  case, the  $qE_r^{\text{self}} + qv_z B_\theta$  pinching force acting on the ions makes  $\phi$  large and negative and the protons move inward to smaller radius and acquire a large transverse momentum. In contrast, when  $\theta_{IRT} = 9^\circ$ , the applied radial electric field nearly compensates for the pinching forces of the self fields in the gap, and thus  $\phi$  and the radial proton excursion are small. If the mean radius of the azimuthal current distribution becomes smaller as the protons move inward and the azimuthal current does not decrease, then the diamagnetic self-field increases.

To determine the radial displacement of the beam, a carbon activation target is placed 15 cm from the cathode. The target consists of narrow annular bands which are counted individually. The number of protons per unit area and the number per radial band as functions of radius are shown in Fig. 4. These graphs are the average of four shots (two shots) for the  $\theta_{IRT} = 9^\circ$  ( $0^\circ$ ) case. The peak voltage is 1.3 MV,  $B_0 = 1.16$  kG, and the total number of protons in the pulse  $N$  is normalized to  $2.3 \times 10^{16}$ . An estimate for  $\phi$  is obtained from  $\tan^{-1} \Delta/15$ , where  $\Delta$  is the distance in cm from the inner edge of the anode to the half-maximum point for linear interpolation between the radial bands. For  $\theta_{IRT} = 0^\circ$ ,  $\phi \approx -15^\circ$ ; for  $\theta_{IRT} = 9^\circ$ ,  $0 > \phi \geq -4^\circ$ .

As a consequence of the large transverse momentum associated with a large  $|\phi|$ , large amplitude radial oscillations of the beam occur downstream from the cusp. Because the guiding center of the orbit is well off axis, the particles come close to the probe assembly (radius 8 mm) and close to the chamber wall. It is estimated that the radial bounce is approximately 16 cm. Therefore, large changes in the radial position of the beam can take place, and the amplitude of  $\delta B_z$  can vary greatly with axial position. Observation of the radial profile of the beam substantiates this explanation. The profiles are measured by nuclear activation analysis of carbon targets. The results for typical shots are illustrated in Fig. 5 where the number per band as a function of radius at axial positions near the probes are shown for  $\theta_{IRT} = 0^\circ$  and  $B_0 = 1.5$  kG ( $\delta$ -configuration). The beam is close to the axis near the  $\delta B_{z1}$  probe. At the  $\delta B_{z2}$  probe, the beam profile is nearly flat and fills the cross-section of the chamber. The average particle radius is larger than at the axial position of the  $\delta B_{z1}$  probe. Further downstream near the third probe, the profile is still nearly flat. However, significant attrition of particles by losses to the wall has occurred. Therefore, the small amplitude of  $\delta B_{z3}$  can be explained by the loss of particles and the radial position of the particles. Because of the radial bouncing of the beam, the ratio  $\xi = \delta B_{z2}/\delta B_{z1}$  depends on  $B_0$ . This is seen in Fig. 6 where  $\xi$  is plotted as a function of  $B_0$ . At low field,  $\xi$  is large; at high field,  $\xi$  is small.

The loss of particles to the chamber wall does not appear to be large in the first meter after the cusp. Typically, the losses are substantially less than 20% in this region. Further downstream, how-

ever, as the diameter of the conical chamber decreases, the losses can be high. These losses depend on the strength of the magnetic field because the mean radial position and the amplitude of the radial bouncing are smaller in a high field. This is illustrated in Fig. 7 where the losses for shot 529 ( $B_0 = 0.99$  kG) and shot 542 ( $B_0 = 1.7$  kG) are shown. These losses are determined by activation analysis of  $10\text{ cm} \times 10\text{ cm}$  carbon targets placed along the chamber wall.

For the lower field case, it is evident from the large losses between 1.0 m and 1.5 m from the cusp that much of the beam is near the chamber wall. In addition, activation analysis of carbon cloth targets wrapped around the on-axis probe assembly shows that 10% of the beam strikes the probe housing between the first and third probe when the first probe is located 50 cm from the cusp.

The effect of the cusp transition width  $\Delta z_c$  on  $\delta B_z$  and the wall losses was investigated. In the normal  $\delta$ -configuration,  $\Delta z_c \approx 60$  cm. This transition width can be reduced to  $\approx 25$  cm by inserting a pair of coils straddling the cusp inside the vacuum chamber. As shown by the comparison of the data for shots 477 and 480 (see Table I), there is little effect on  $\delta B_z$ . Similarly there is no significant difference in the losses to the wall. This insensitivity to  $\Delta z_c$  is probably the result of the overwhelming influence of the self-fields on the motion in the cusp. For shot 480,  $\zeta_1 \approx 1.67$ . Thus, gross distortion of the cusp field occurs.

A series of experiments was performed to maximize the ratio  $v_u/v_z$ . Since the available stored energy of the capacitor bank was insufficient to produce the desired magnetic field for the high injection energy, the potential applied to the anode of the IRT (which could be as high as 1.5 MV) was reduced to 0.7 - 0.9 MV. From the time delay  $\Delta\tau$  of the half-amplitude points of the leading edge of the magnetic probe signals, it has been determined that the axial energy downstream from the cusp is less than 50% of the injection energy. Since the energy invested to build-up the self fields is small in comparison with the kinetic energy, it is reasonable to assume that the transverse energy is comparable to the longitudinal energy. The maximum value obtained for the ratio  $v_u/v_z$  is 1.5 and is achieved in the  $\delta$  configuration with  $B_0 = 1.7$  kG for an injection energy of 0.9 MeV.

Tests with the steeper gradient  $\kappa$ -configuration of the applied magnetic field did not result in an appreciable change in  $v_1/v_z$  as determined from measuring  $\Delta\tau$  for the leading edge. However, the width of the  $\delta B_z$  signals increases with axial position because of the difference in  $v_z$  at the head and the tail of the beam. Specifically, in the  $\kappa$ -configuration with  $B_0 = 2.9$  kG,  $\delta B_{z1}$  lasts  $\sim 65$  nsec and  $\delta B_{z2}$  has a plateau on the trailing edge and a pulse width of  $\sim 116$  nsec (FWHM). The  $\Delta\tau$  between the half-maximum points of the trailing edge indicates that  $v_z \sim 0.45$  cm/nsec corresponding to an energy of 0.1 MeV. Thus, it is likely that a substantial fraction of the protons in the pulse have  $v_1/v_z$  greater than the value obtained for the particles at the leading edge of the pulse.

To further increase the ratio  $v_1/v_z$ , the IRT was modified to produce a larger radius beam. Because the radial magnetic field  $B_r$  at the cusp increases proportionally to  $r$ , the azimuthal force experienced by a charged particle passing through the cusp is proportional to  $r$ . Therefore, higher rotational velocities can be obtained by increasing the radius of the beam. The anode of the new source is a 48 cm i.d., 58 cm o.d., 150  $\mu$ m thick polyethylene ring. In a limited number of shots taken with  $\theta_{\text{IRT}} = 0^\circ$ , the source typically produces  $\sim 1.0\text{--}1.5 \times 10^{16}$  protons per pulse. From activation analysis of carbon targets, it has been estimated that  $|\phi| < 12^\circ$ . A new magnetic field configuration,  $\lambda$ , is employed to provide a steep gradient and high magnetic mirror peak.

With the large radius beam, a substantially reduced  $v_z$  is observed downstream from the cusp. For  $B_0 = 1.27$  kG ( $\lambda$ -configuration) and  $V_0 \sim 0.98$  MV, the  $\Delta\tau$  between the half-maximum points on the leading edge of  $\delta B_{z1}$  (at 40 cm from the cusp) and  $\delta B_{z2}$  is  $\sim 70$  ns. This corresponds to  $v_z \sim 0.71$  cm/nsec from which an energy of  $\sim 0.27$  MeV is inferred. At  $B_0 = 1.6$  kG, and  $V_0 \sim 1.08$  MV, the  $\Delta\tau$  is nearly the same. In this case  $v_1/v_z \sim 1.7$ .

The results of this series of experiments unequivocally demonstrate that the ratio  $v_1/v_z$  can be increased to the desired level provided that the appropriate magnetic field is used.

Especially interesting is the shape of the  $\delta B_z$  signals. The  $\delta B_{z1}$  signal for  $B_0 = 1.27$  kG is narrow, ( $\sim 60$  nsec FWHM) and has a second peak delayed by  $\sim 120$  nsec from the first and about one-third of

its amplitude. For  $B_0 = 1.6$  kG, the second peak of  $\delta B_{z1}$  is almost as large as the first and is delayed by  $\sim 40$  ns. The  $\delta B_{z1}$  signal has a width of  $\sim 120$  nsec (FWHM). For both values of  $B_0$ ,  $\delta B_{z2}$  has a single peak, but its amplitude is  $\sim 40\%$  smaller for the higher field. A possible explanation is that the second peak in the  $\delta B_{z1}$  signal is the result of reflected particles. If the reflection point for the  $B_0 = 1.27$  kG case is near the axial position of  $\delta B_{z2}$ , then no second peak would appear in  $\delta B_{z2}$ . Also observed is that the interval between the peaks is about twice the  $\Delta\tau$  measured between  $\delta B_{z1}$  and  $\delta B_{z2}$ . At the second probe (90 cm from the cusp)  $B_{z2} \sim 6.6$  kG. In the higher field case, the same field strength occurs at 67 cm from the cusp. Therefore, based on the limited data set available, it appears that the shape of the  $\delta B_z$  signal is consistent with reflection of a large fraction of the particles in the beam.

### (b) Computer Simulation

The dynamics of a proton layer launched into the applied magnetic field configuration used in the experiment are investigated by computer simulation. This study uses a particle-in-cell code which has been described previously<sup>28-30</sup> and is similar to several other codes which have been used to study field-reversed configurations.<sup>31-34</sup> The code has cylindrical axisymmetry ( $r, z$ -geometry), and includes the self- and external-  $B_z$  and  $B_r$  magnetic field components and the inductive  $E_\theta$  electric field. These fields are derived from the azimuthal component of the vector potential  $A_\theta(r, z, t)$  which is calculated from the self-consistent azimuthal current density by solving the equation,

$$\nabla^2 A_\theta - A_\theta/r^2 = -\mu_0 J. \quad (1)$$

The protons are space charge neutralized by background or accompanying electrons, and there are no axial or radial currents.

Solution for  $A_\theta$  is obtained on a  $32 \times 128$  grid by Fourier analysis in the  $z$ -direction and by Gaussian elimination in  $r$ . At the boundaries,  $A_\theta$  is set equal to zero because the time scales of interest are shorter than the time for the magnetic field to penetrate the chamber wall. The size of a cell is adjustable providing that  $\Delta_z/\Delta_r < 8$  for numerical accuracy, where  $\Delta_{z(r)}$  is the length of the cell in the  $z(r)$  direction.

The proton layer is represented by 2000-10000 macro-particles which are injected into the specified external B with assigned canonical angular momentum  $P_\theta$ . The invariance of  $P_\theta$  is used to calculate the azimuthal velocity  $v_\theta$  at a given particle position. The total particle energy (kinetic and field) is monitored and energy conservation to within 1% is found.

The initial conditions for the proton beam at injection are chosen to model the beam at the cathode of the IRT. The protons are launched with a specified energy and a given injection angle  $\phi(r)$ , that is computed from

$$\phi(r) = \frac{r - r_0}{r_2 - r_0} \phi_m, \quad (2)$$

where  $|\phi_m| = |\phi(r_2)|$  is the maximum value of  $|\phi(r)|$  and  $\phi(r_0) = 0$ . The protons that are emitted toward the virtual cathode and which reflect before reaching the grid and then pass through the hole in the anode can be included in the beam by selecting an anode inner radius  $r_1$  that is less than the true inner radius of the anode plastic. If these protons have slightly divergent velocities, then  $r_0 > r_1$  can be chosen.

Both the proton current and the potential applied to the anode are approximated by triangular pulses (see Fig. 8). The potential rises from an initial value of 400 kV to a peak value  $V_0$  and then falls to a terminal potential of 400 kV. Both waveforms have a pulse width of 60 nsec.

At various times during the simulation run the code computes the mean energy, "fluid" velocity components and contour maps of important quantities such as particle density, current density,  $A_\theta^{\text{total}}$ ,  $A_\theta^{\text{self}}$  and  $B_z^{\text{self}}$ . In addition, the field lines are plotted, and the particle flux as a function of radius is obtained for a few axial positions. This allows a comparison to be made between the computer simulation and the experiment of the location of the particle dump on the wall, the beam radial profile, the diamagnetic signal on axis and at the wall.

Although the code is generally in good agreement with the experimental observations, it should be noted that several aspects of the experimental conditions have been ignored in the simulation.

including electrostatic fields, the inductive axial electric field, and the electron dynamics. Also missing from the code are the converging chamber walls and the removal from the system of particles that would strike the wall in the experiment.

The radial profile of the proton beam predicted by the simulation is shown in Fig. 9. The 1.2 MeV, 120 kA, proton pulse is produced from an anode with  $r_2 = 18.5$  cm and  $r_1 = 4.5$  cm  $= r_0$  with  $\phi_m = -10^\circ$  and  $-15^\circ$ . The anode is located 30 cm upstream from the cusp, and the pulse propagates in the  $\delta$ -configuration with  $B_0 = 1.4$  kG. The position of the experimental chamber wall is shown, although the code assumes the wall is at  $r = 33$  cm for all axial positions.

As expected, at 15 cm before the cusp, the outer edge of the proton beam is displaced inward by  $l \tan \phi_m$ , where  $l$  is the distance between the target and the anode. After the cusp, however, it is seen that  $\phi$  has a strong influence on the radial position of the protons and on the loss rate to the wall. At 50 cm from the cusp, the profile of the  $15^\circ$  case is broader but also has a smaller inner radius. The profiles for both cases are peaked further from the axis in the downstream targets. The protons in the  $15^\circ$  case move outward so far that between 1.0 and 1.4 m from the cusp that they hit the wall.

A comparison of a simulation for  $\phi_m = -15^\circ$  and several experimental shots is shown in Fig. 10. For both computer results and experiment, the number of protons per unit area is plotted as a function of radius. In the simulation,  $2.25 \times 10^{16}$  protons are emitted from an anode with  $r_2 = 16.5$  cm,  $r_1 = 2$  cm, and  $r_0 = 3$  cm. The 1.2 MeV, 120 kA, proton pulse is injected into the magnetic configuration with  $B_0 = 1.4$  kG. At 15 cm distance before the cusp, the computed profile is in good agreement with the data of shot 597 for which  $N_p = 2.5 \times 10^{16}$  protons. Downstream from the cusp, the comparison is made with the available data from shots with a smaller  $N_p$ . To make the comparison with the simulation, the data from these shots (#602, 604, 607) have been normalized to  $N_p = 2.5 \times 10^{16}$ . In Fig. 10, the normalized data is plotted, but the actual  $N_p$  is also given for each case. Although the coarse resolution of the experimental points makes the agreement in amplitude less precise, the width predicted by the simulation at 50 cm from the cusp is approximately the same as that observed in the experiment. Further downstream the agreement is good at small radius but breaks down at large radius. However, it

is clear from the simulation that significant loss to the wall occurs between 100 cm and 141 cm from the cusp. The integrated particle flux which strikes the wall of the vacuum chamber agrees with the results of activation analysis of wall targets.

Both the shape and amplitude of the on-axis diamagnetic signals predicted by the simulation are in fair agreement with those observed experimentally at various axial positions. For example, the simulation gives  $\delta B_{z1} \sim 1.5$  kG,  $\delta B_{z2} \sim 0.5$  kG, and  $\delta B_{z3} \sim 0.35$  kG. The experimentally observed values are  $\delta B_{z1} \sim 2.0$  kG,  $\delta B_{z2} \sim 0.2$  kG, and  $\delta B_{z3} \sim 0.06$  kG. The low value of  $\delta B_{z1}$  predicted by the computer is apparently the result of the oversimplified model of the initial conditions. At the position of the first probe, the radial distribution of azimuthal current and thus  $\delta B_z$  are rapidly varying functions of axial position. Small errors in the initial conditions can cause a large discrepancy in  $\delta B_{z1}$ . In contrast, the predicted values of  $\delta B_{z2}$  and  $\delta B_{z3}$  are too high. This is largely due to the fact that the code does not remove particles from the beam once they strike the wall of the vacuum chamber.

The radial bouncing motion of the beam is evident in the contour plots of the azimuthal current density  $J_\theta(r,z)$  in the  $r$ - $z$  plane. An example is given in Fig. 11 for a beam with  $V_0 = 0.85$  MV,  $I_p = 90$  kA, and  $\phi_m = -15^\circ$ . Contours of  $J_\theta$  are shown in snapshot frames. The first frame is at 60 nsec after the beginning of emission of the proton pulse, and succeeding frames are spaced by 60 nsec intervals. The protons are emitted from an anode with  $r_2 = 18.5$  cm, and  $r_0 = 4.5$  cm. The chamber wall radius is 33 cm and the position of the conical chamber wall used in the experiment is shown as a reference.

In the figure, an arrow indicates the location(s) of maximum current density, and its magnitude is given in each frame. The current density decreases by 20% of the maximum value between successive contours in directions away from the peak current density. Since five contours are plotted in each frame, there is an order of magnitude difference in current density from the highest to lowest contour.

In the 60 nsec frame, the entire pulse has been emitted. Most of the particles are moving inward. The outer edge of the beam has become concave, and the density is peaked near the head of the beam. The peak  $J_\theta$  is near a radius of 19 cm, and the average particle radius is 7.1 cm. At 120 nsec, the head

of the beam has spread outward radially, and has very steep gradients near the leading edge. A long wake has developed at the tail. The head extends along the radial direction from 4.5 cm to 18 cm, and the average radius is 12.5 cm. The mean axial velocity is 1.1 cm/nsec and the average  $v_\theta/v_z \approx 0.26$ . In the third frame, at 180 nsec, the head of the beam fills the entire cross section of the chamber (average particle radius is 11.2 cm) and particles are intercepted by the wall. In addition, the wake of slower particles in the tail is lengthening. In the 240 nsec frame, an appreciable fraction of the beam has bumped into the wall.

A high magnetic field and smaller injection angle reduce the amplitude of the radial oscillation of the beam. Results of a simulation using the  $\delta$ -configuration with  $B_0 = 4$  kG are shown in Fig. 12. Plotted are  $J_\theta$  contours in the  $r$ - $z$  plane for a beam with  $V_0 = 0.85$  MV,  $I_p = 90$  kA, and  $\phi_m = -8.6^\circ$ . Key features include the formation of a steep gradient at the head of the pulse and a long wake at the tail. In the third and fourth frames (180 nsec and 240 nsec) reflected particles are seen, and the axial motion of the dense part of the pulse is slow. The average  $v_z$  is  $\sim 7.3$  mm/nsec and  $v_\theta/v_r \sim 1.1$  at 180 nsec. In agreement with the experimental results, the simulation predicts small wall losses for these injection conditions.

The influence of self fields on the propagation velocity is most apparent for simulations of higher current beams. As reported earlier,<sup>28</sup> the self field produces a somersaulting, i.e., particles at the head of the beam are decelerated and particles at the tail are accelerated. The result is a spreading of the distribution of particle energy. Another effect of the self field is to reinforce the cusp at the outer radius and to weaken it at the inner radius of the beam. Particles at the inner edge of the beam thus do not rotate as much as a single particle would in the absence of the self field. At the outside of the beam, the particles see a stronger cusp and gain a greater azimuthal velocity.

These effects are demonstrated in the results of a simulation of a 350 kA beam ( $V = 1.3$  MV,  $\phi_m = -15^\circ$ ,  $B_0 = 1$  kG,  $\delta$ -configuration). The distortion of this cusp is apparent in Fig. 13, where the field lines of the combined self and applied fields are displayed in the  $r$ - $z$  plane. Reconnection occurs

before the wake of slower particles has passed the midplane of the cusp. Shown in Fig. 14 are contours of proton density at various times after the proton emission begins. The peak density region and highest gradient are near the head of the beam. A long wake of slower particles forms quickly, and a large radial expansion of the beam envelope occurs between 1.0 m and 1.9 m downstream from the cusp. The mean ratio  $v_{\theta}/v_z$  increases along the ramp to  $\sim 0.3$  at 2 m, and the average  $v_z$  slows from 1.36 cm/nsec at 20 cm after the cusp to 1.17 cm/nsec at 1.95 m downstream from the cusp. However, the head of the pulse actually accelerates along the ramp. Just past the exit of the cusp  $v_z \approx 1.16$  cm/nsec for the head of the beam. Between 50 cm and 90 cm from the cusp, the leading edge averages  $v_z \sim 1.6$  cm/nsec, and between 90 cm and 1.75 m, the head moves with  $v_z \sim 1.7$  cm/nsec. Thus the motion of the leading edge corresponds to an energy about 10% greater than the peak applied potential. In contrast, the average total velocity  $\sim 1.3$  cm/nsec corresponds to an energy of  $\sim 1.0$  MV that is less than the average potential applied to the IRT anode.

The larger radius beam propagated in the  $\lambda$  configuration has also been simulated. A simulation was performed with  $V_p = 1$  MV,  $I_p = 50$  kA,  $1.0 \times 10^{16}$  protons/pulse,  $B_0 = 2.3$  kG,  $r_2 = 29$  cm,  $r_1 = 24$  cm, and  $\phi_m = -10^\circ$ . The current density contours are shown in Fig. 15. Large inward radial motion is observed in the first 100 nsec. The average radius for the two frames shown is 15.3 cm (100 nsec) and 13.9 cm (200 nsec). At 100 nsec, the average  $v_z$  is  $\sim 6.4$  mm/nsec and  $v_{\theta}/v_z \sim 1.6$ . A substantial fraction of the beam reflects between 50 cm and 75 cm from the cusp so that at 200 nsec the average  $v_z$  is negative ( $\sim -0.5$  mm/nsec). Also the temporal shape of the computed  $\delta B_{z1}$  and  $\delta B_{z2}$  agree with the experiment, although both are somewhat higher. The simulation predicts  $\delta B_{z1} = 660$  G at 50 cm from the cusp and  $\delta B_{z2} \sim 180$  G. For  $B_0 = 1.6$  kG, the value for  $\delta B_{z1}$  is about three times the observed value, and the predicted  $\delta B_{z2}$  is about twice that of the experiment. The discrepancy between experiment and simulation is probably the result of differences in the initial and boundary conditions and perhaps the neglect of electron dynamics. In particular, the value of  $\delta B_z$  is extremely sensitive to the radial position of the beam which in turn is sensitive to the injection angle and applied field.

#### IV. INTERACTION WITH NEUTRAL GAS

The propagation of the rotating layer along the ramp in the presence of a low density neutral gas background was investigated. The purpose of these experiments was to study the formation of an azimuthal plasma return current and to test the coupling between the motion of the beam and the plasma currents. The experiments with neutral gas are performed by injecting a puff of neutral gas ( $N_2$  or air) into the conical portion of the vacuum chamber. Fast opening valves of the magnetically-driven-hammer type are used.<sup>36</sup> The valves are mounted on the chamber 1.5 m from the cusp. After the valves are opened, the gas cloud expands at approximately the sonic speed. When the front of the cloud reaches a desired axial position, the potential pulse is applied to the IRT and the beam is launched. The pressure is monitored by an electron receiving tube (type 5702) operated as a fast ionization gauge.<sup>37</sup> Pressure front risetimes are typically less than 1 msec. The main diagnostic measurements of the beam propagation are observations of the diamagnetic signals and the prompt  $\gamma$ -ray pulse from a teflon target located 200 cm downstream from the cusp.

When the pressure of neutral gas is greater than 100 mTorr, azimuthal plasma return currents are excited that almost completely neutralize the azimuthal proton current. This is illustrated in Fig. 16 where on-axis  $\delta B_z$  signals with and without gas are shown. In addition, a small axial slowing of the layer also occurs when it interacts with gas. The time of flight to a Teflon target located 200 cm from the cusp is (determined from the half maximum point on the leading edge of the prompt  $\gamma$ -ray signals)  $\sim 140$  nsec without gas and  $\sim 175$  nsec with gas. For the shot without gas, the inferred average axial velocity is 1.64 cm/nsec which is nearly equal to the initial velocity of particles with the peak injected energy  $\sim 1.4$  MeV. For the shot with gas, the average  $v_z$  is  $\sim 1.3$  cm/nsec corresponding to about 0.9 MeV.

A large radial expansion of the beam follows its azimuthal current neutralization. As a result, a substantial number of particles strike the wall. This dump onto the walls begins within a half meter of the front of the gas cloud.

It is apparent from the results of Figs. 16 and 17 that in the presence of a background gas cloud, the  $\delta B_z$  signals exhibit oscillation and change of sign. In Fig. 17, the  $\delta B_{z1}$  is large because the neutral gas arrives at the position of the probe after the proton pulse. The  $\delta B_{z1}$  signal has a long tail that is attributed to the clamping of the field by the high conductivity plasma. The period of oscillation is longer for  $\delta B_{z2}$  (1.4  $\mu$ sec) than for  $\delta B_{z3}$  (450 nsec).

The observed periods are consistent with the excitation of magnetosonic waves.<sup>38</sup> The theory<sup>39</sup> predicts that the period of this mode is

$$\tau_m \approx \frac{2a}{V_A} \left[ 1 + \frac{(\pi c)^2}{(L\omega_{pi})^2} \right]^{1/2} \approx \frac{2a}{V_A}, \quad (3)$$

where  $V_A$  is the Alfvén speed,  $a$  is the beam radius,  $L$  is a characteristic length and  $\omega_{pi}$  is the ion plasma frequency. The plasma density  $n_p$  can be estimated from  $2n_0 \Gamma_b \sigma \tau$ , where  $n_0$  is the background density,  $\Gamma_b$  is the average proton flux of the beam,  $\sigma$  is the ionization cross section  $\sim 1.2 \times 10^{-16}$  cm<sup>2</sup>, and  $\tau$  is the pulse duration  $\sim 50$  nsec. The factor of 2 accounts for the ionization by the co-moving electrons. Typically  $n_p \sim 2.5 \times 10^{13}$ /cm<sup>3</sup> for a background pressure of  $\sim 100$  mTorr. For shots 521 and 511, the values of the external field at the position of the probes are  $B_{z1} = 2.4$  kG,  $B_{z2} = 3.5$  kG, and  $B_{z3} = 5.9$  kG. The estimated values  $V_A$  are  $2.8 \times 10^7$ ,  $4.1 \times 10^7$ , and  $6.9 \times 10^9$  cm/sec and  $a = 10$ , 18, and 17 cm respectively. Equation (3) predicts  $\tau_m = 0.7$ , 0.9 and 0.5  $\mu$ sec. In view of the imprecision in the estimate of  $n_p$ , the values of  $\tau_m$  are in approximate agreement with the experimental values.

An upper bound can be calculated for the electron-ion collision frequency  $\nu_{ei}$  from the theoretical<sup>40,41</sup> stopping length  $l$  given by

$$l \approx \frac{1}{2} \frac{n_p}{n_b} \left( \frac{v_z}{v_b} \right)^2 \frac{v_z}{\nu_{ei}}, \quad (4)$$

where  $n_p/n_b \sim 10$ ,  $v_z/v_b \sim 4$ , and  $v_z = 1.2 \times 10^9$  cm/sec. From the experimental observation that the beam has lost about 1/3 of the energy associated with its axial motion in a distance of 200 cm,  $l \geq 400$  cm. This length implies  $\nu_{ei} < 10^9$  sec<sup>-1</sup>. Critical damping of the wave requires

$$\nu_{ei} \geq 2\omega_{IH} \left( 1 + \frac{\omega_{pe}^2}{c^2 k^2} \right)^{1/2}, \quad (5)$$

where  $\omega_{IH}$  is the lower hybrid frequency,  $\omega_{pe}$  is the electron plasma frequency and  $k = \pi/a$  is the wavenumber. If  $n_p = 2 \times 10^{13}/\text{cm}^3$ , and  $a = 10$  cm, Eq. (5) gives the  $\nu_{ei} \sim 1.5 \times 10^{10}$  B (B in kG). Because the value of  $\nu_{ei}$  determined from the stopping distance is much less than this value, the mode is underdamped, as it is observed experimentally.

Recently reported results of the ion ring experiment at Cornell University include the observations that (1) the azimuthal plasma return current is absent in  $\text{H}_2$  or  $\text{D}_2$  background gas but it is present with He,  $\text{N}_2$ , or air background gas, and (2) the diamagnetic signals have oscillatory tails that change sign.<sup>42</sup> These results are also consistent with the excitation of magnetosonic oscillation. For a nitrogen plasma of density  $\sim 1 \times 10^{14}$ ,  $B_z \sim 8$  kG, and  $a = 13$  cm the predicted period of the oscillations is  $\sim 0.43$   $\mu\text{sec}$ . This value is within a factor of 1.5 of the observed period. For a hydrogen gas background, the plasma density is probably less than for  $\text{N}_2$  by about a factor of 3. Therefore in hydrogen gas, for  $B_z = 8$  kG, the period is  $\sim 66$  nsec. Because this period is less than the pulse length, the plasma return current is expected to be small as observed experimentally.

## V. SUMMARY

The experimental observations show that the amplitude of the radial oscillations downstream from the cusp depends strongly upon the initial conditions and, in particular, the injection angle  $\phi$ . These oscillations, in turn, influence  $\delta B_z$  and the loss of particles to the wall. Injection into the cusp at large radius and with a high field and steep ramp result in a ratio  $v_u/v_z \sim 1.7$  and in the reflection of a substantial fraction of the pulse.

Computer simulation of the experiment also indicates the effect of  $\phi$  on the radial bouncing. Good agreement is obtained between computed and observed radial profiles at various axial positions. The code predicts the axial position and magnitude of the losses to the wall, and the predicted amplitude of  $\delta B_z$  is in approximate agreement with the experimental measurements. Simulation for high

field and moderate  $\phi$  reveals low losses to the walls, reflection of some of the particles as well as the large  $v_{th}/v_z$  observed for large radius injection.

Furthermore, during the interaction of the layer with neutral gas at moderate pressure, the azimuthal beam current is neutralized by the beam excited plasma current. The observed oscillatory behavior of the diamagnetic signals can be explained by assuming the excitation of the magnetosonic mode.

In conclusion, the main features of the dynamics of a field-reversed rotating proton layer along a magnetic ramp are reasonably well understood. It appears that suitable magnetic field configurations can sufficiently slow the axial motion of the layer to permit the formation of a stationary, field-reversed proton ring that can be used to confine plasma.

#### Acknowledgments

The authors are grateful for the dedicated technical assistance given by R. A. Covington, J. J. Negri, E. A. Bellafiore, and J. W. Snider.

Funding has been provided by the Office of Naval Research and by the Department of Energy.

#### REFERENCES

1. N.C. Christofilos, Proc 2nd U.N. International Conf. on Peaceful Uses of Atomic Energy, IAEA, Vienna, **32**, 279 (1958).
2. K.R. Chu and C.A. Kapetanakis, Nucl. Fus. **15**, 947 (1975).
3. D.S. Prono, J.W. Shearer, and R.J. Briggs, Proc. International Top. Conf. on Electron Beam Research and Technology, Albuquerque, N.M., Vol. 1, p. 575 (1975).
4. H.H. Fleischmann, Proc. U.S.-Japan Joint Symposium on Compact Toruses and Energetic Particle Injection, Princeton, p. 41 (1979); also H.H. Fleischmann, Proc. 3rd Symposium on Physics and

Technology of Compact Toroids in the Magnetic Fusion Energy Program, Los Alamos, p. 31 (1980).

5. R.N. Sudan, Phys. Rev. Lett. **41**, 476 (1978).
6. H.H. Fleischmann, Annals of N.Y. Acad. of Sci. **251**, 472 (1975); also H.H. Fleischmann and T. Kammash, Nucl. Fus. **15**, 1143 (1975).
7. R.N. Sudan and E. Ott, Phys. Rev. Lett. **33**, 355 (1974).
8. A.C. Smith, et al., Report 78 Fus-1, Pacific Gas and Electric Co., San Francisco, CA (1978).
9. R.V. Lovelace, Phys. Fl. **22**, 549 (1979).
10. C.A. Kapetanacos, Memorandum Report 4093, NRL, Washington, D.C. (October 1979).
11. P. Sprangle and C.A. Kapetanacos, J. Appl. Phys., **49**, 1 (1978).
12. M.L. Andrews, H. Davitian, H.H. Fleischmann, B. Kusse, R.E. Kribel, and J.A. Nation, Phys. Rev. Lett. **27**, 1428 (1971); also see H.H. Fleischmann, IEEE Trans. on Nuc. Sci. **NS-20**, 966 (1973).
13. C.A. Kapetanacos, R.K. Parker, K.R. Chu, Appl. Phys. Lett., **26**, 284 (1975).
14. N.C. Christofilos, in Proc. of the 2nd International Conf. on the Peaceful Uses of Atomic Energy, Geneva, 1958 (United Nations, NY, 1959) **32**, p. 279.
15. J. Rand McNally, Jr., ORNL Report No. TM-4965, 1975 (unpublished).
16. C.A. Kapetanacos, J. Golden, and F. Young, Nucl. Fus., **16**, 151 (1976).
17. S. Humphries, C. Eichenberger and R.N. Sudan, J. Appl. Phys. **48**, 2738 (1977); also P.L. Dreike, D.A. Hammer, R.N. Sudan, and L.G. Wiley, Phys. Rev. Lett., **41**, 1328 (1978).

18. J. Golden, C.A. Kapetanakis, S.J. Marsh, and S.J. Stephanakis, *Phys. Rev. Lett.*, **38**, 130 (1977).
19. J.A. Pasour, R.A. Mahaffey, J. Golden, and C.A. Kapetanakis, *Appl. Phys. Lett.*, **36**, 646 (1980).
20. P. Dreike, C. Eichenberger, S. Humphries, Jr., and R. Sudan, *J. Appl. Phys.*, **47**, 85 (1976).
21. D.J. Johnson, G.W. Kuswa, A.V. Farnsworth, Jr., J.P. Quintenz, R.J. Leeper, E.J.T. Burns, and S. Humphries, Jr., *Phys. Rev. Lett.*, **42**, 610 (1979).
22. C.A. Kapetanakis, J. Golden, J.A. Pasour, S.J. Marsh, and R.A. Mahaffey, *Phys. Rev. Lett.*, **44**, 1218 (1980).
23. J.B. Greenly, P.L. Dreike, D.A. Hammer, P.M. Lyster, Y. Nakagawa, R.N. Sudan, *Proc 3rd Symposium on Physics and Technology of Compact Toroids*, 2-4 Dec. 1980, Los Alamos Scientific Lab., Rept LA-8700-C (1980).
24. J.A. Pasour, J. Golden, C.A. Kapetanakis, *Proc. 1980 IEEE Int. Conf. on Plasma Sci.*, No. 80CH 1544-6 NPS, p. 96 (1980).
25. D.E. Pershing, J. Golden, J.A. Pasour, S.J. Marsh, and C.A. Kapetanakis, submitted to *J. Appl. Phys.*, (1981).
26. F.C. Young, J. Golden, and C.A. Kapetanakis, *Rev. Sci. Instrum.* **48** 432 (1977).
27. J. Golden, R.A. Mahaffey, J.A. Pasour, F.C. Young, and C.A. Kapetanakis, *Rev. Sci. Instrum.* **49**, 1384 (1978).
28. S.J. Marsh, A.T. Drobot, J. Golden, C.A. Kapetanakis, *Phys. Rev. Lett* **39**, 705 (1977).
29. S.J. Marsh, A.T. Drobot, J. Golden, C.A. Kapetanakis, *Phys. Fl.* **21**, 1045 (1978).
30. S.J. Marsh, A.T. Drobot, C.A. Kapetanakis, *Plasma Phys.* (to be published 1981); also Rept. 4297, NRL, Washington, D.C. (1980).

31. M. Brettschneider, J. Killeen, A.A. Marin, J. Comput. Phys. **11**, 360 (1973).
32. J.A. Byers, J.P. Holdren, J. Killeen, A.B. Langdon, A.A. Marin, M.E. Rensink, C.G. Tull, Phys. Fl. **17**, 2061 (1974).
33. J.A. Byers, Phys. Rev. Lett **39**, 1476 (1977).
34. A. Friedman, R.L. Ferch, R.N. Sudan, A.T. Drobot, Plasma Phys. **19**, 1101 (1977).
35. F.C. Young, F. Oliphant, and S.J. Stephanakis, Rept. 4171, NRL Washington, D.C. (1980).
36. A. Fisher, F. Mako, J. Shiloh, Rev. Sci. Instrum., **49**, 872 (1978).
37. J. Valsamakis, Rev. Sci. Instrum. **37**, 1318 (1966).
38. C.A. Kapetanacos, W.M. Black, K.R. Chu, Phys. Rev. Lett **34**, 1156 (1975).
39. K.R. Chu, C.A. Kapetanacos, R.W. Clark, Appl. Phys. Lett **27**, 185 (1975).
40. K. Molvig and N. Rostoker, Phys. Fl. **20**, 494 (1977).
41. K. Molvig and N. Rostoker, Phys. Fl. **20**, 504 (1977).
42. P.L. Dreike, Ph.D. Thesis: "Formation, Propagation, and Reflection of a Rotating Proton Ring in a Magnetic Mirror," Cornell University, Ithaca, N.Y. (Aug. 1980).

Table 1 — Data for Selected Shots

m.c.*	$B_o$ (kG)	$\delta B_{z1}$ (kG)	$\delta B_{z2}$ (kG)	$\delta B_{z3}$ (kG)	Shot
$\delta$	1.16	0.15	0.04	0.02	475a
$\delta$	1.27	2.18	0.69	0.09	381
$\delta$	1.02	2.18	1.01	0.32	477
$\delta^+$	1.05	2.56	1.28	—	480
$\eta$	1.32	1.66	0.19	—	557
$\eta$	1.20	1.92	0.12	—	585
$\eta$	1.19	2.24	0.38	0.19	558
$\eta$	1.14	1.64	0.15	—	563
$\delta$	0.69	2.18	1.76	0.58	541b
$\delta^+$	0.76	2.21	1.26	0.45	484b
$\delta^+$	1.05	2.18	1.35	0.75	482b
$\delta^+$	1.46	2.27	0.15	0.06	485b
$\delta$	1.7	1.4	0.23	—	542b

\*m.c. = magnetic configuration

 $\delta$  cusp width  $\approx 50$  cm $\delta^+$  cusp width  $\approx 25$  cma  $\theta_{IRI} = 9^\circ$  (other shots  $\approx 0^\circ$ )

b anode i.d. = 9.5 cm (other shots = 18 cm)

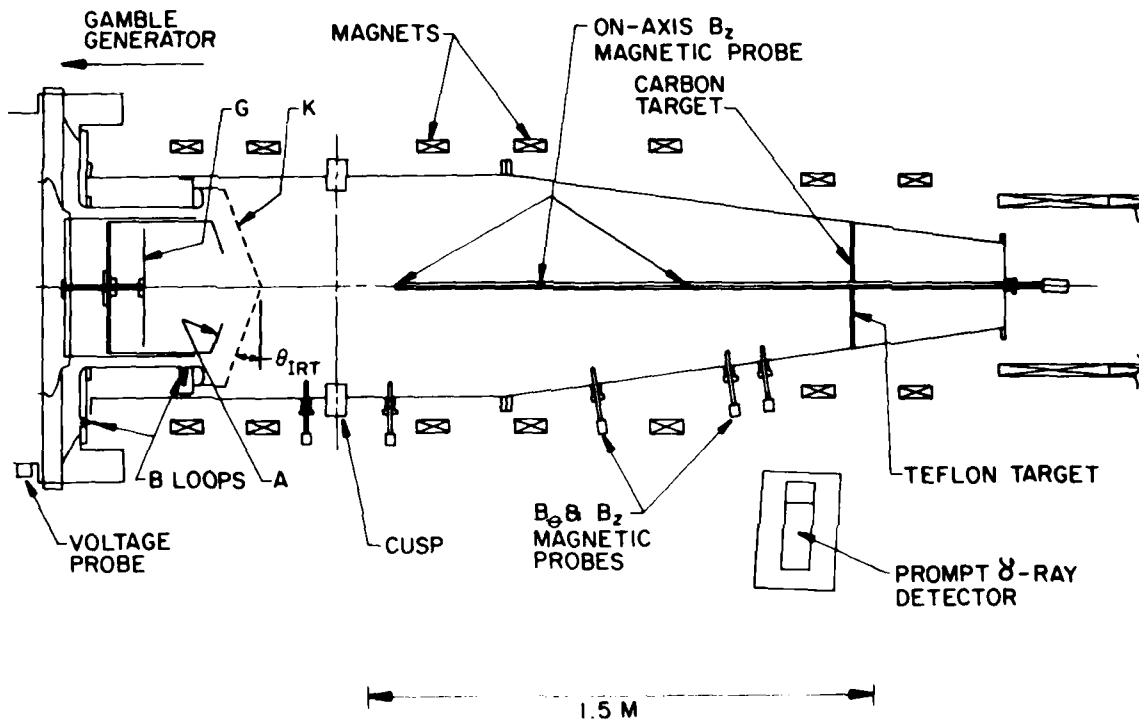


Fig. 1 - Schematic of experiment and associated diagnostics

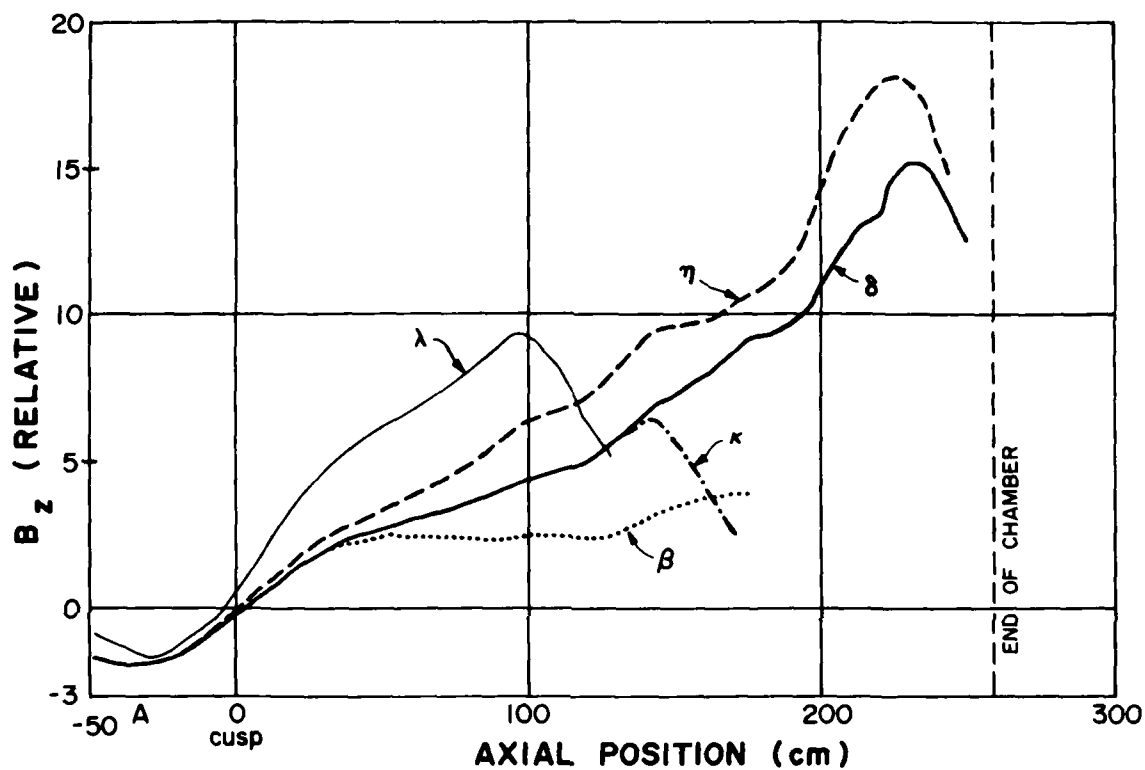


Fig. 2 — Several applied magnetic field configurations used in the experiments

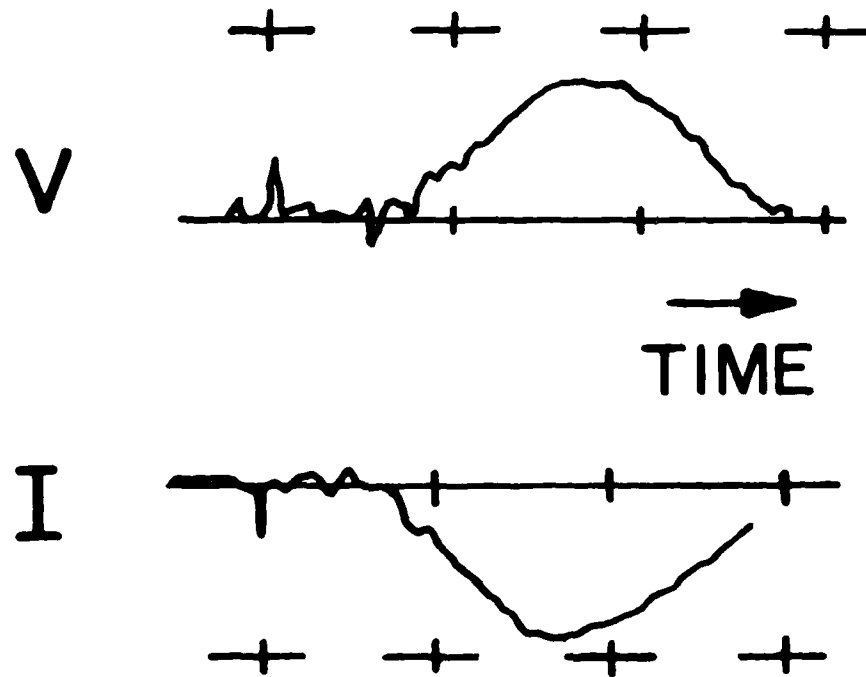


Fig. 3 — Typical voltage (inductively corrected) and current (reversed polarity) waveforms for the IRT. Voltage scale: 2.4 MV/div. Current scale: 1.0 MA/div. Time scale for both waveforms: 60 nsec/div.

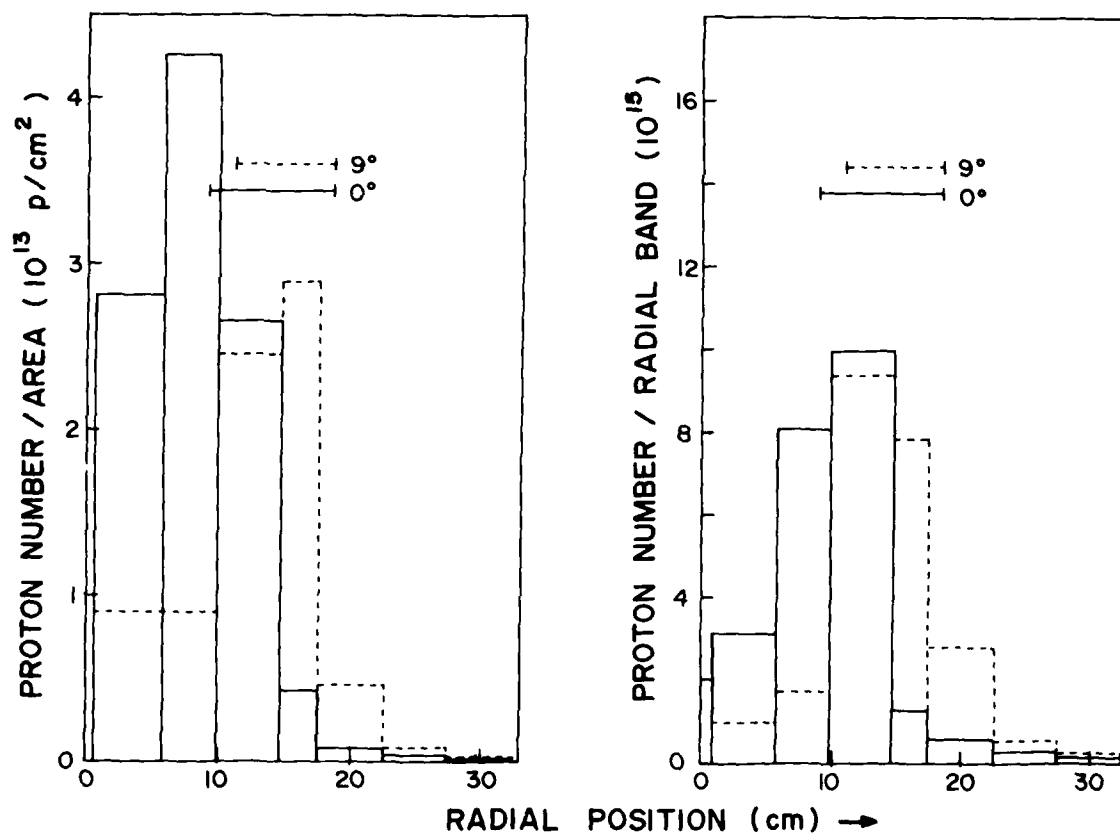


Fig. 4 — Number of protons per unit area and the number per radial band striking a segmented carbon target 15 cm from the cathode ( $\sim 15$  cm before the cusp) with  $B_0 = 1.16$  kG. The two cases are for a planar IRT ( $\theta_{\text{IRT}} = 0^\circ$ ) and for a conical IRT ( $\theta_{\text{IRT}} = 9^\circ$ ). The radial extent of the anode is indicated for each case.

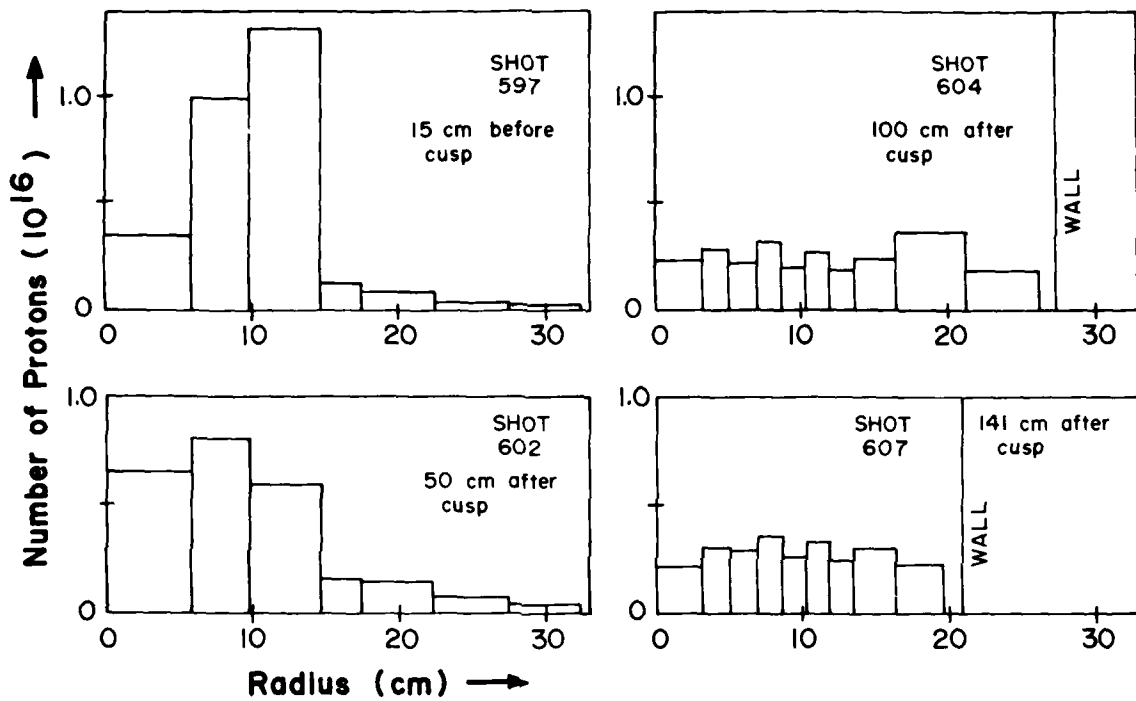


Fig. 5 — Radial profiles of proton beam at various axial positions for  $\theta_{\text{IRI}} \approx 0^\circ$  and  $B_0 = 1.5$  kG (6-configuration).

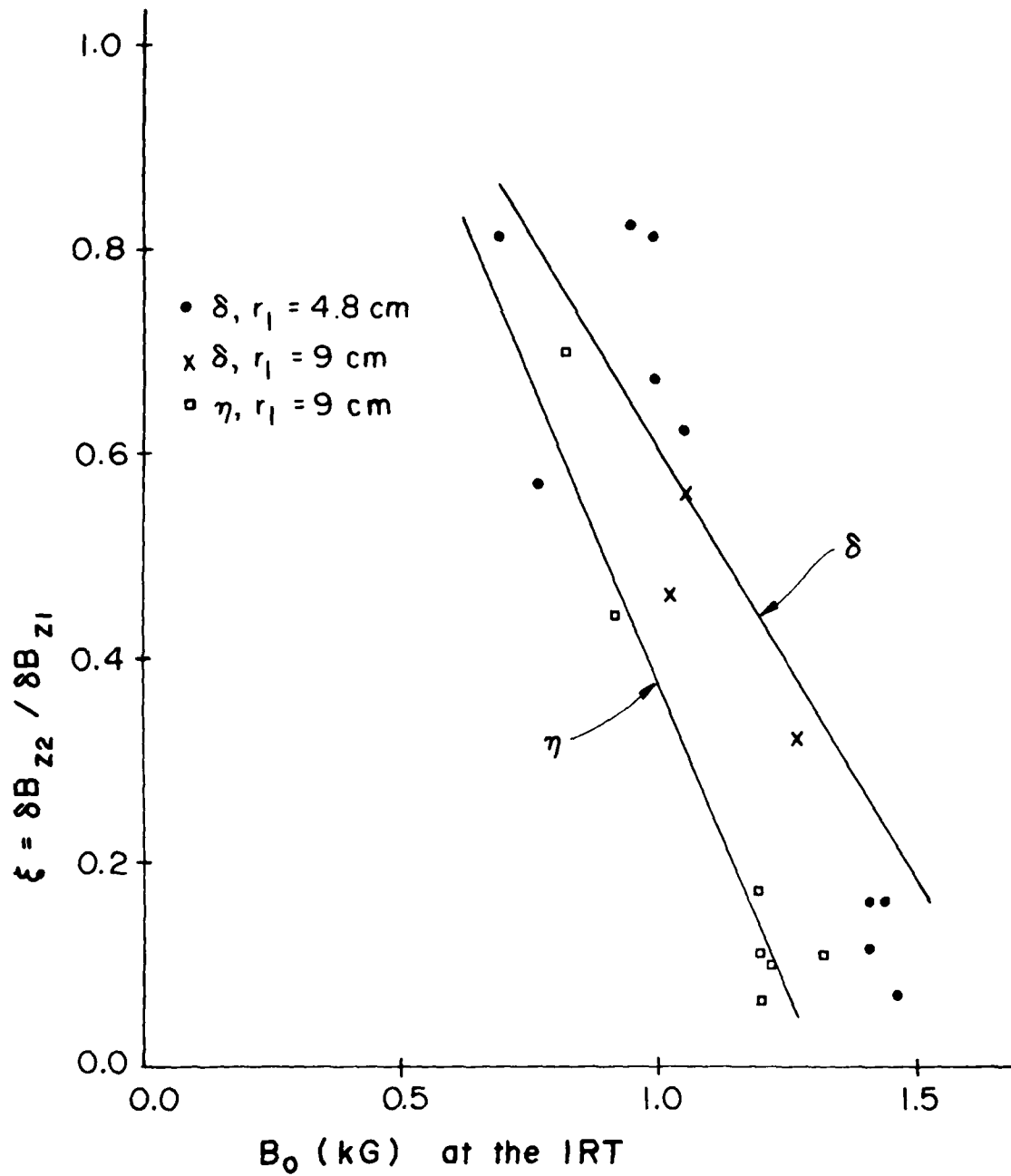


Fig. 6 — Ratio of on-axis diamagnetic field 100 cm from cusp to that 50 cm from cusp for two field configurations. The lines are least square fits, and the anode inner radius  $r_1$  is given for each case.

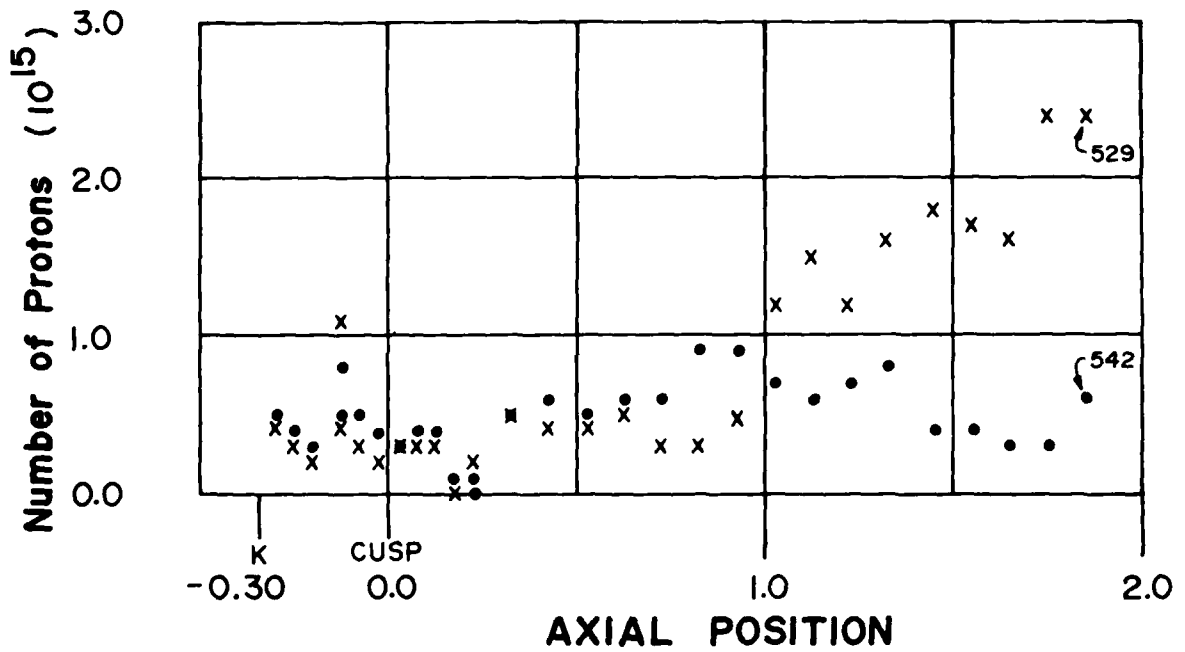


Fig. 7 — Number of protons per 10 cm axial band lost to wall vs axial position. For shot 529,  $B_0 = 0.99$  kG. For shot 542,  $B_0 = 1.7$  kG. Both shots,  $\delta$ -configuration.

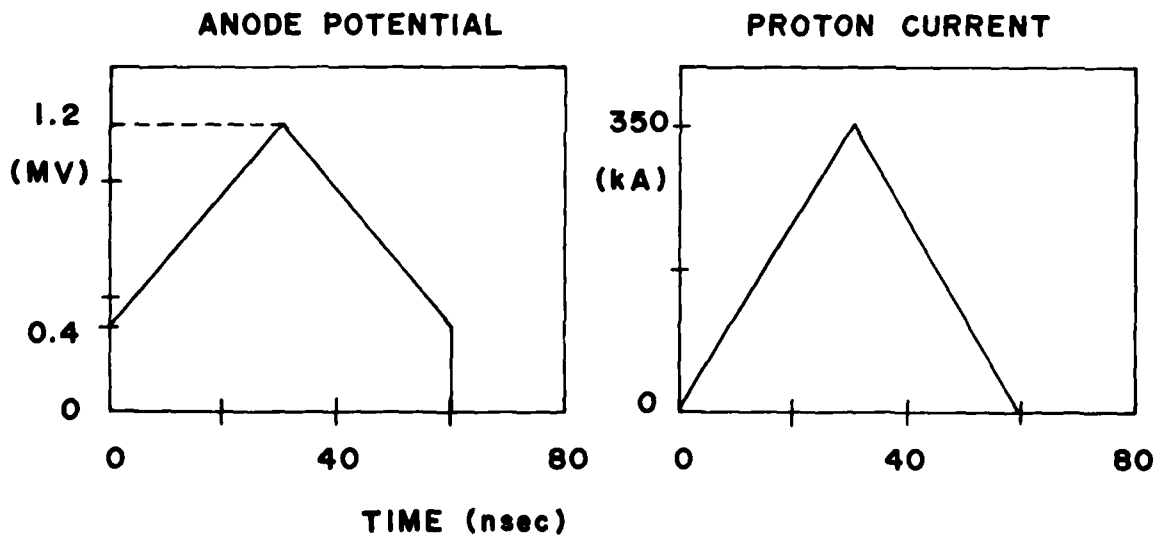


Fig. 8 — Idealized applied anode voltage and proton current waveforms used in computer simulations

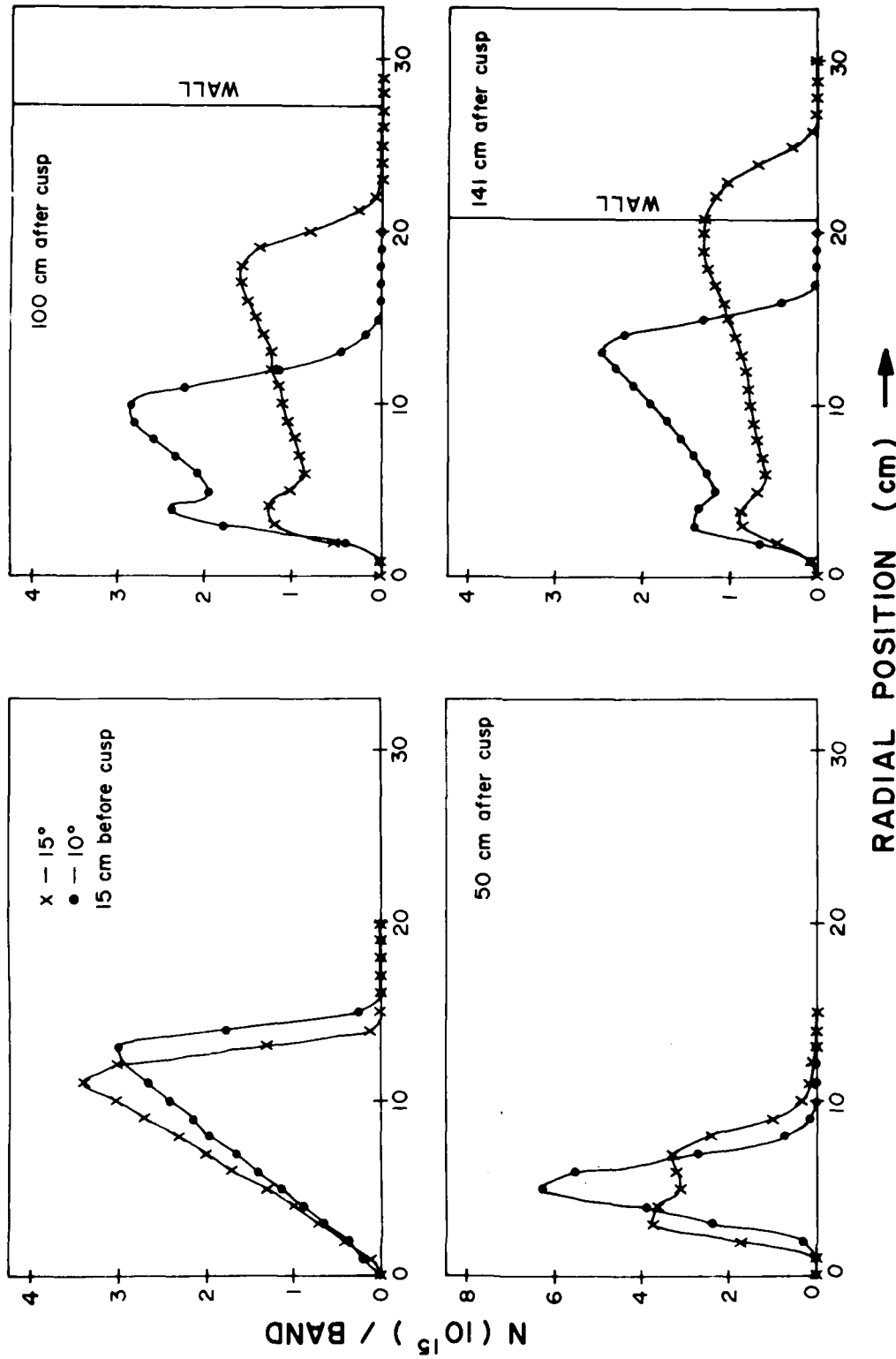


Fig. 9 — Number of protons per 1 cm radial band at various axial positions and for maximum injection angles of 10° and 15°. Data is from simulation with  $V_0 = 1.2$  MV,  $I_p = 1.20$  kA, and  $B_0 = 1.4$  kG (6-configuration)

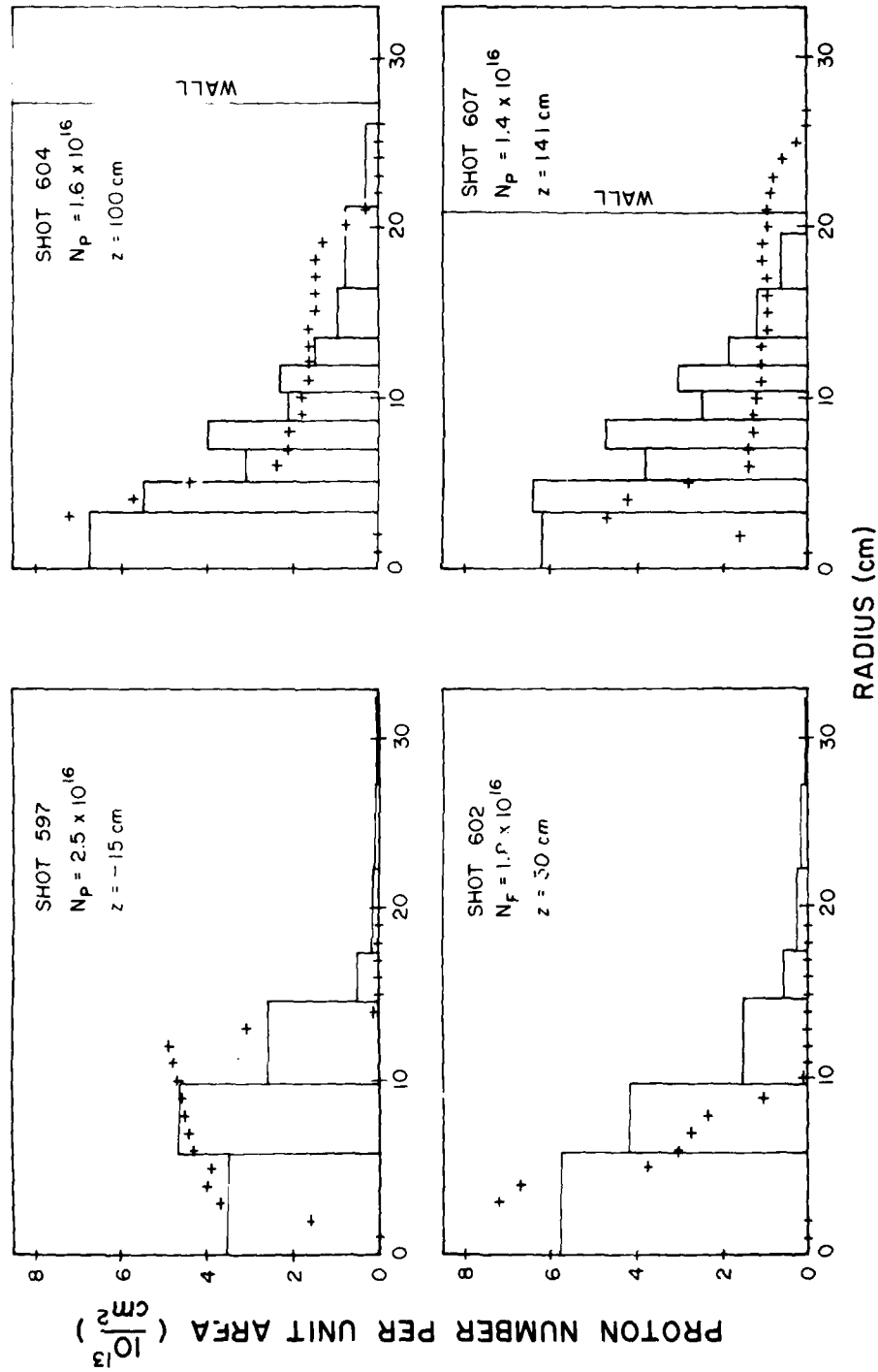


Fig 10 - Comparison of simulation and experimental radial profiles at various axial positions. In the simulation,  $V_0 = 1.2$  MV,  $I_p = 120$  kA ( $N_p = 2.25 \times 10^{16}$ ) and  $\phi = 15^\circ$ . In both the simulation and the experiment,  $B_0 = 1.4$  kG (6-configuration). The peak voltage is 1.2 MV on all shots except No. 604 where  $V_0 = 1.4$  MV. The experimental data are normalized to  $N_p = 2.5 \times 10^{16}$  for comparison with the simulation, but the measured  $N_p$  is also given.

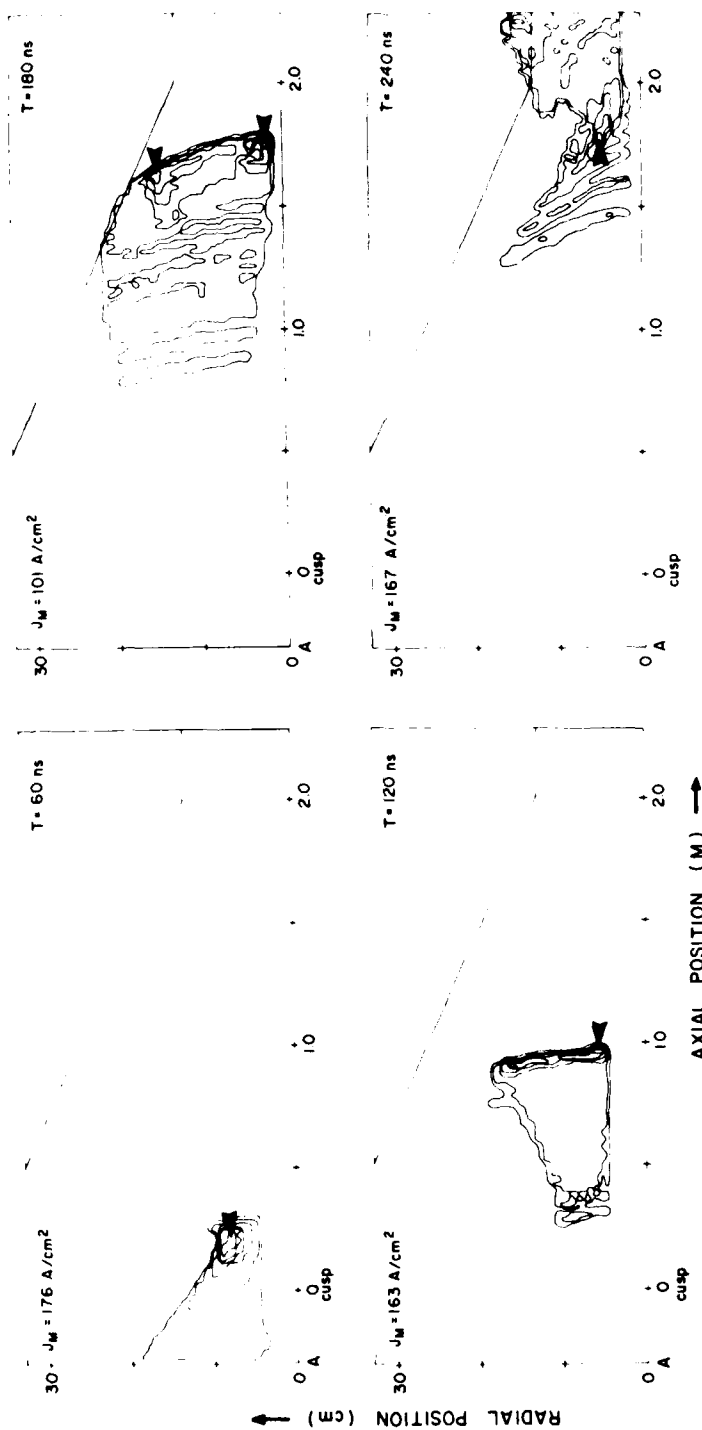


Fig. 11 — Contours of  $J_M$  at various times after the beginning of proton emission from simulation with  $V_0 = 0.85$  MV,  $I_p = 90$  kA,  $\phi_m = -15^\circ$ , and  $B_0 = 1.75$  kG (8-configuration). Each contour line represents a change of 20% of the maximum current density  $J_M$  at that time. The arrows show the position(s) of  $J_M$  at each time.

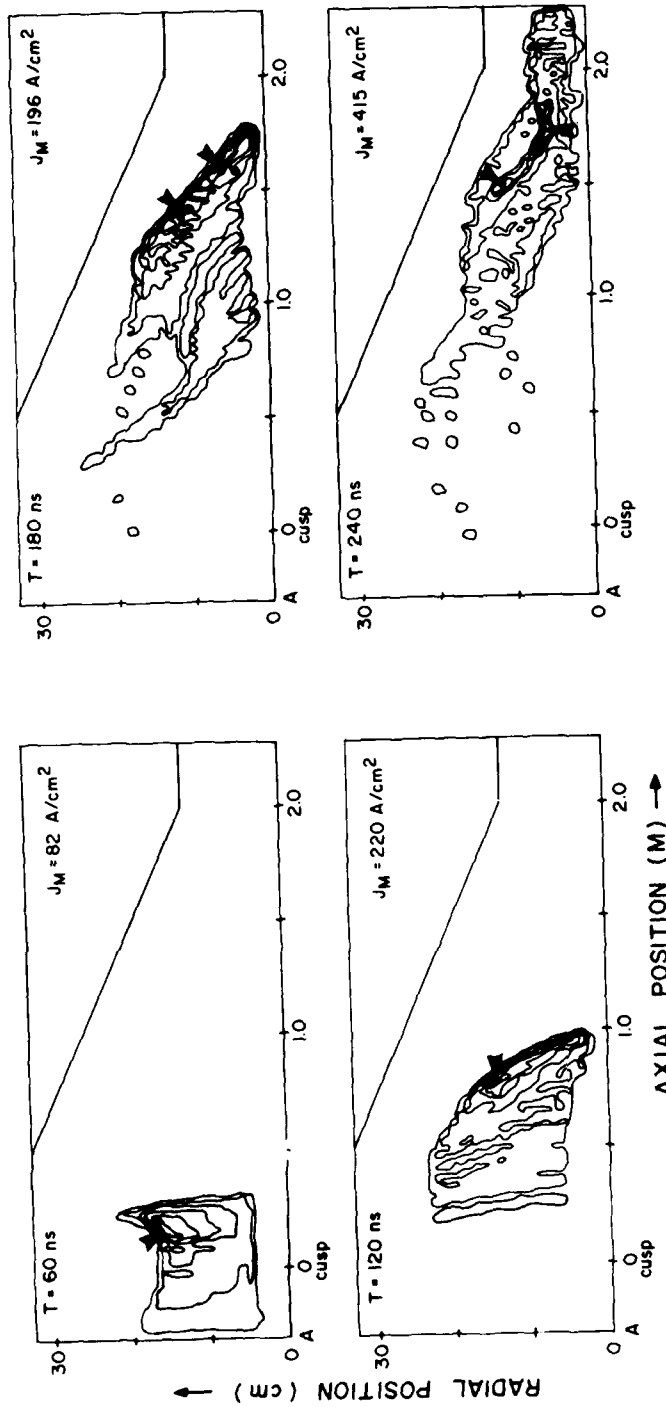


Fig 12 — Contours of  $J_M$  at various times after proton emission at high magnetic field:  $B_0 = 4$  kG ( $\delta$ -configuration). The simulation uses  $V_0 = 0.85$  MV,  $I_p = 90$  kA, and  $\phi_m = -8.6^\circ$ . Arrows represent location(s) of maximum current density  $J_M$ , which is given for each frame. Each contour line represents a change of  $0.2 J_M$ .

NRL Ion Ring Experiment

Computer simulation of a  $I_p = 350$  kA,  $E_p = 1.2$  MeV proton pulse passing through a magnetic cusp.

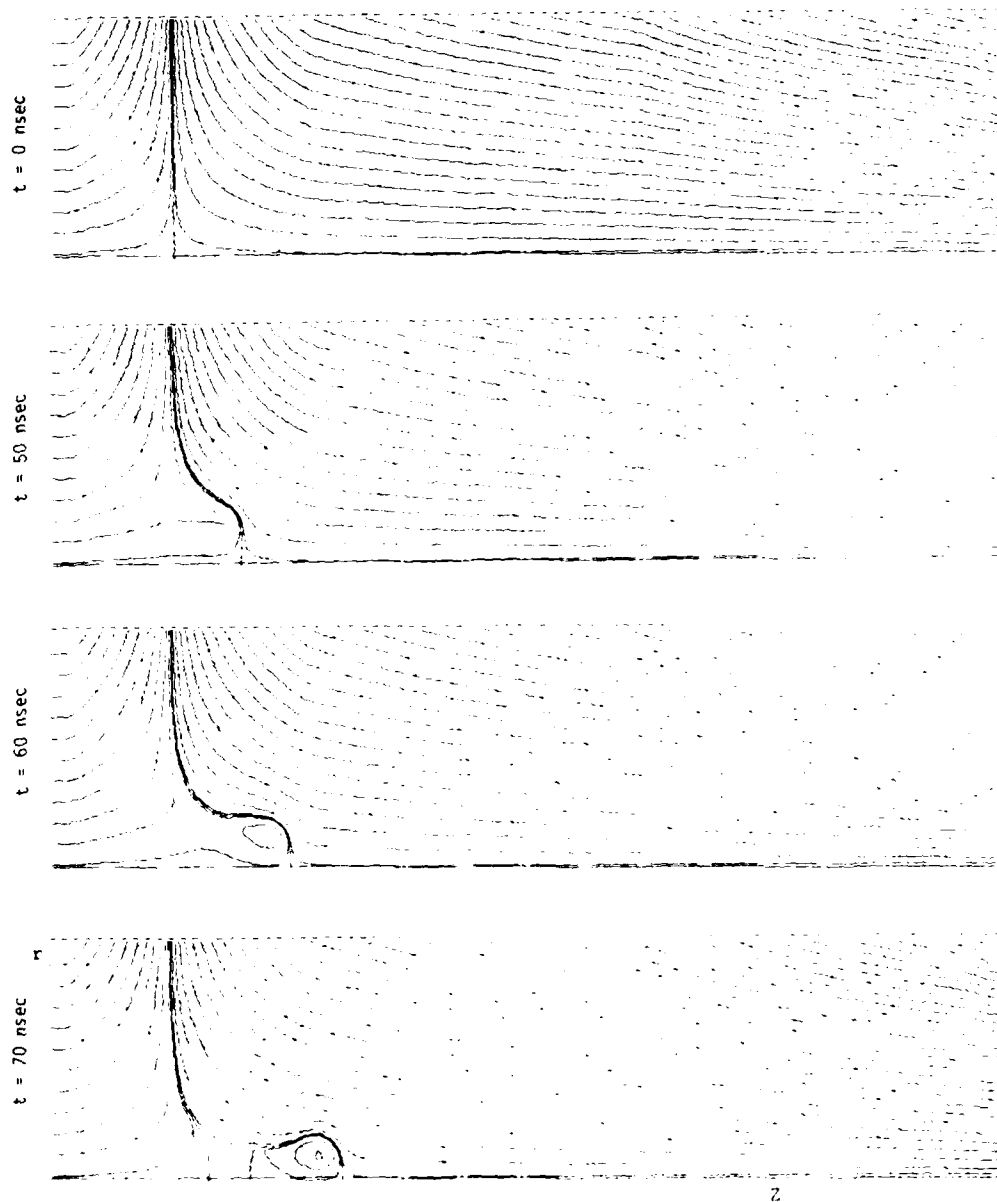


Fig. 13 — Lines of total magnetic field ( $B_{ext} + B_{self}$ ) at various times after proton emission, as calculated by simulation with  $V_0 = 1.2$  MV,  $I_p = 350$  kA,  $\phi_m = 15^\circ$ ,  $B_0 = 1$  kG (6-configuration)

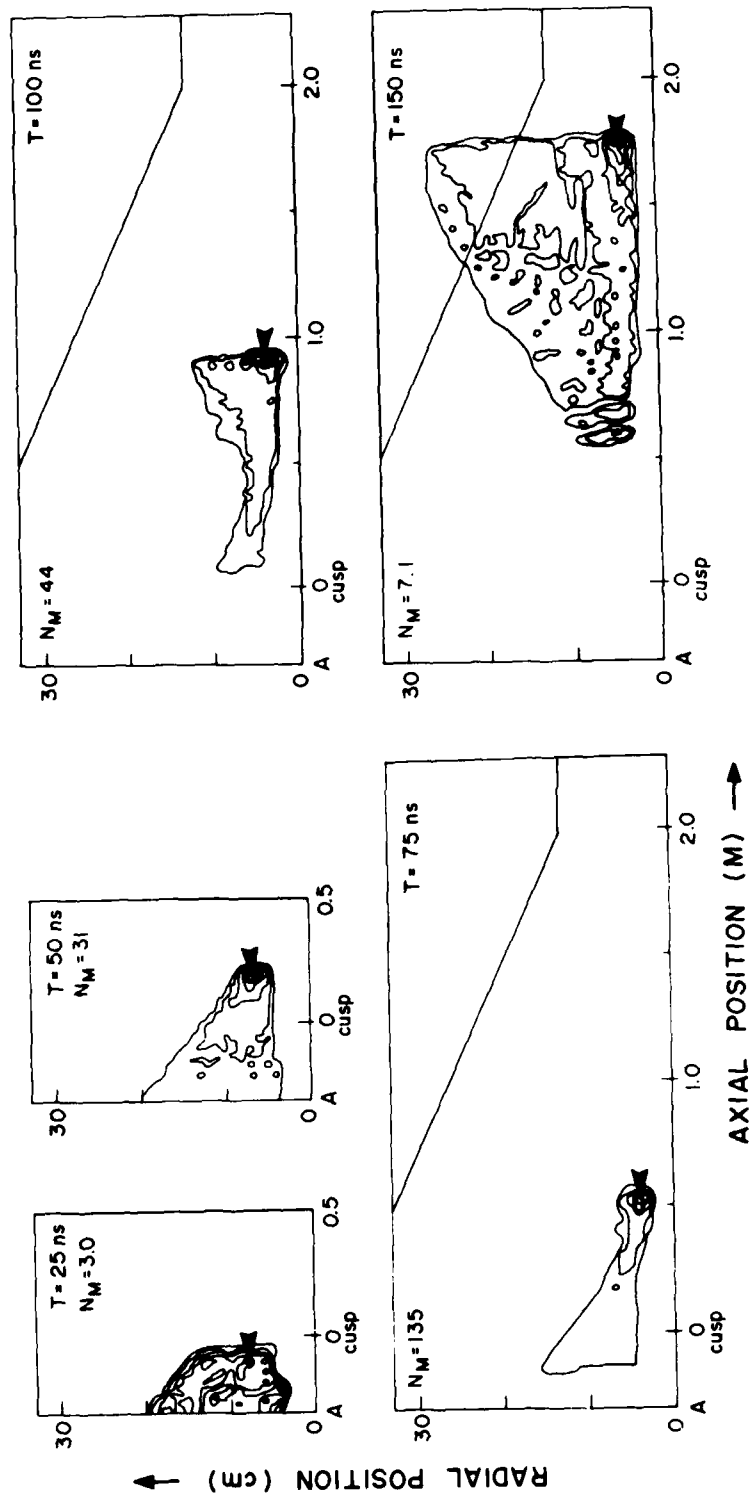


Fig. 14 — Proton density contours for the simulation used for Fig. 13. Arrows locate maximum density  $N_M$ , which is given in units of  $10^{12} \text{ cm}^{-3}$ , and each contour line represents a change of  $0.2 N_M$ .

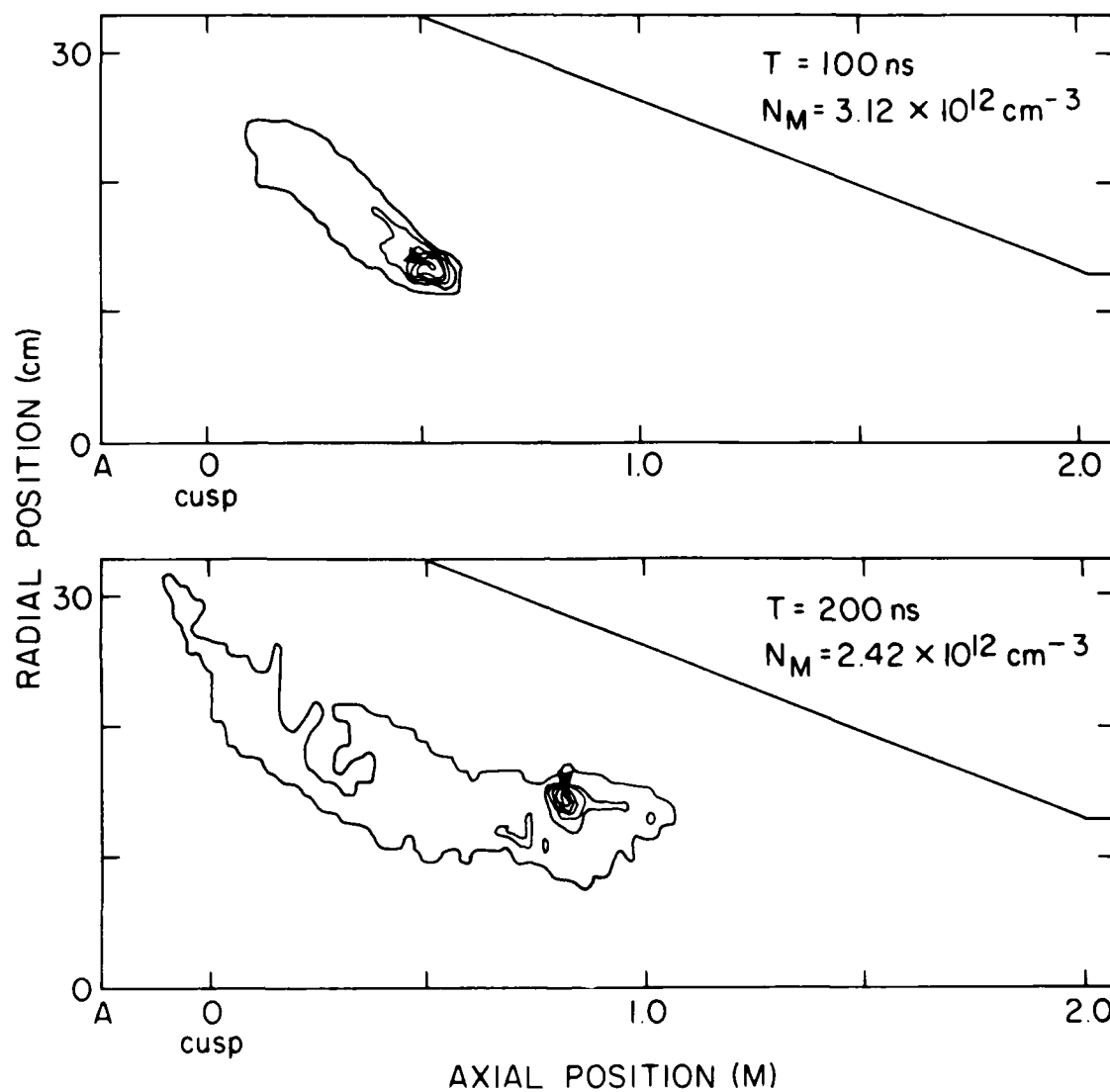
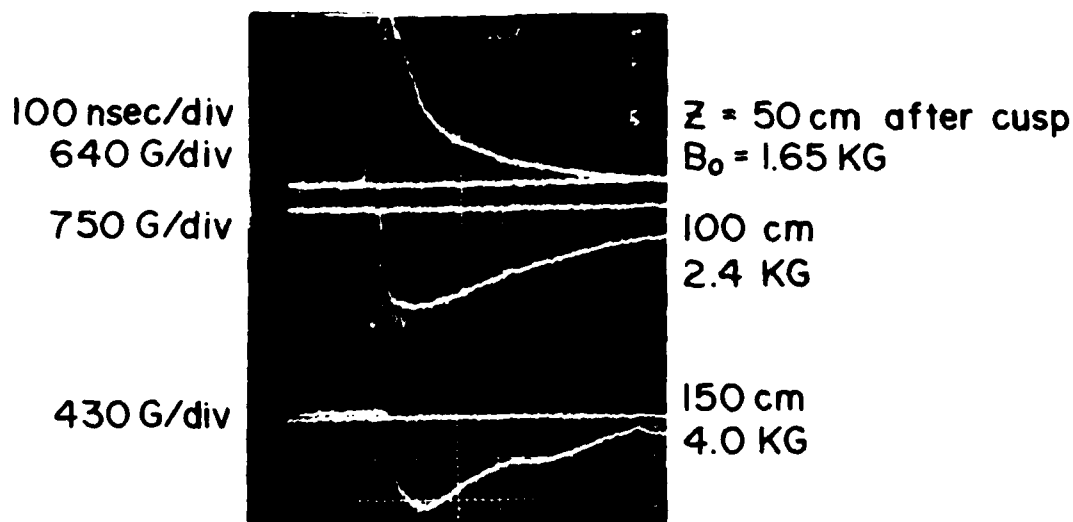


Fig. 15 - Proton density contours from simulation using a large diameter IRT ( $r_2 = 29 \text{ cm}$ ,  $r_1 = 24 \text{ cm}$ ) and a large, steeply ramped magnetic field ( $B_0 = 2.3 \text{ kG}$ , A-configuration). Here  $V_2 = 1 \text{ MV}$ ,  $I_p = 50 \text{ kA}$ , and  $\phi_m = -10^\circ$ . Arrows locate maximum density  $N_M$ , and each contour represents a change of  $0.2 N_M$ .

### Shot 493

No Gas



### Shot 521

$N_2$  Gas ( $P \sim 100$  mTorr)

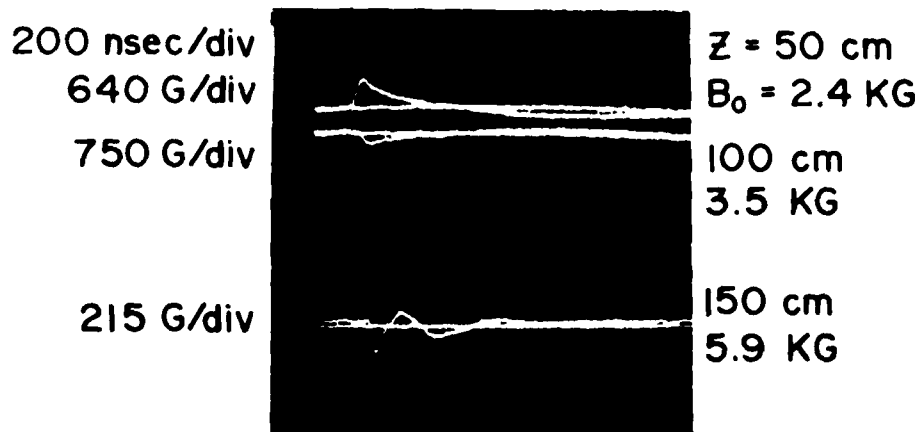
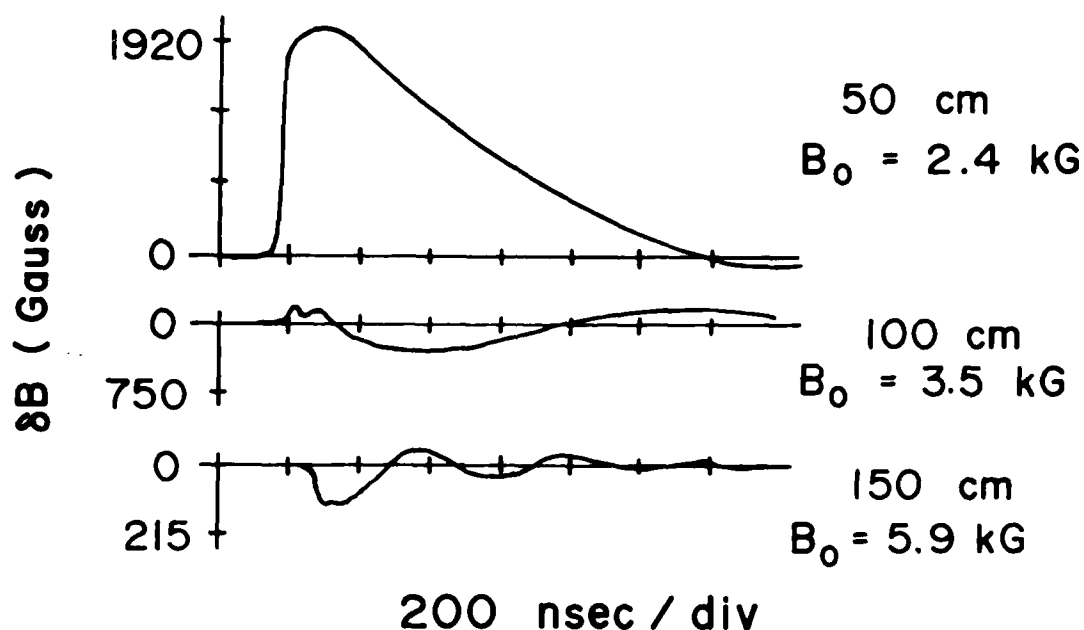


Fig. 16 — Diamagnetic signals on axis from a shot without gas and a shot with gas. The top trace in each set has its polarity reversed at the scope for display purposes. In shot 521, the front of the gas cloud is located  $\sim 30$  cm downstream from the cusp.

## DIAMAGNETIC SIGNALS WHEN GAS FRONT AT $Z \approx 45$ CM



Shot 511  
 $N_2$  (  $P \sim 200$  mTorr )

Fig. 17 — Diamagnetic signals on axis from a shot in which the gas front (  $\sim 200$  mTorr air ) has just reached the first probe (  $\sim 50$  cm from cusp ).

DISTRIBUTION LIST

Dr. M. Allen  
Stanford Linear Accelerator Center  
Stanford, CA 94305

Dr. W.G. Applegate  
CIA  
Washington, DC 20505

Dr. R. Avery  
Lawrence Berkeley Laboratory  
Berkeley, CA 94720

Dr. W. Barletta  
Lawrence Livermore National Laboratory,  
P.O. Box 808  
Livermore, CA 94550

Dr. M. Barton  
Brookhaven National Laboratory  
Upton, L.I., NY

Dr. J. Bayless  
DARPA ATTN: DEO  
1400 Wilson Blvd.  
Arlington, VA 22209

Dr. Jim Benford  
Physics International Co.  
2700 Merced St.  
San Leandro, CA 94577

Dr. Kenneth Bergerson  
Plasma Theory Division - 5241  
Sandia National Laboratories  
Albuquerque, NM 87115

Prof. A. Bers  
Department of Electrical Engineering  
Mass. Inst. of Technology  
77 Massachusetts Ave.  
Cambridge, MA 02159

Dr. V.M. Birttritsky  
Lenina 2a  
Research Institute of Nuclear Physics  
Tomsk, USSR

Dr. Daniel Bix  
Lawrence Livermore National Laboratory,  
P.O. Box 808  
Livermore, CA 94550

Dr. A.E. Blaugrund  
Weizman Institute of Science  
Rohovot, Israel

Dr. Charles Brau  
Los Alamos Scientific Laboratory  
Los Alamos, NM 87544

Dr. R. Briggs  
Lawrence Livermore National Laboratory,  
P.O. Box 808  
Livermore, CA 94550

Dr. Allan Bromborsky  
Harry Diamond Laboratory  
2800 Powder Mill Road  
Adelphi, MD 20783

Dr. M. Butram  
Sandia National Laboratory  
Albuquerque, NM 87115

Dr. J.M. Buzzi  
Ecole Polytechnique  
Plateau de Palaiseau  
91120 Palaiseau, France

Dr. M. Caponi  
TRW Advance Tech. Lab.  
1 Space Park  
Redondo Beach, CA 90278

Dr. P.J. Castleberry  
Defense Intelligence Agency  
ATTN: DT-IA  
Washington, DC 20301

Prof. F. Chen  
Department of Electrical Engineering  
University of California  
at Los Angeles  
Los Angeles, CA 90024

Dr. D. Chernin  
c/o Code 4790  
Naval Research Laboratory  
Washington, DC 20375

Dr. Blake E. Cherrington  
Department of Electrical Engineering  
University of Illinois  
Urbana, IL 61801

Dr. Jen Chang Chou  
Institute of Nuclear Energy Research  
P.O. Box 3  
Lung-Tan, Taiwan

Dr. W. Condit  
Division of Applied Plasma Physics  
Department of Energy  
Washington, DC 20545

Prof. G. Contopoulos  
Department of Astronomy  
University of Athens  
Athens, Greece

Dr. Charles C. Damm  
Lawrence Livermore National Laboratory,  
P.O. Box 808  
Livermore, CA 94550

Prof. B. Dangor  
Department of Physics  
Imperial College of Science and Technology  
London, S.W. 7 ENGLAND

Prof. R. Davidson  
Plasma Fusion Center  
Massachusetts Institute of Technology  
Cambridge, MA 02139

Dr. J. Dawson  
University of California at Los Angeles  
Department of Physics  
Los Angeles, CA 90024

Dr. W.N. Destler  
Department of Electrical Engineering  
University of Maryland  
College Park, MD 20742

Dr. A.N. Didenko  
Institute of Nuclear Physics  
Tomsk, USSR

Prof. W. Doggett  
North Carolina State University  
P.O. Box 5342  
Raleigh, NC 27650

Dr. H.J. Doucet  
Director  
Laboratoire de Physique des Milieux Ionises  
Ecole Polytechnique  
Plateau de Palaiseau  
91120 Palaiseau, France

Dr. W. Dove  
Department of Energy  
Washington, DC 20545

Dr. H. Dreicer  
Director Plasma Physics Division  
Los Alamos Scientific Laboratory  
Los Alamos, NM 87544

Prof. W.E. Drummond  
Austin Research Associates  
1901 Rutland Drive  
Austin, TX 78758

Dr. J.G. Eden  
Department of Electrical Engineering  
University of Illinois  
155 EEB  
Urbana, IL 61801

Dr. W.E. Ellis  
Chief Magnetic Mirror Systems  
Office of Fusion Energy  
Department of Energy  
Washington, DC 20545

Dr. R.J. Faehl  
Los Alamos Scientific Laboratory  
Los Alamos, NM 87544

Dr. A. Faltens  
Lawrence Berkeley Laboratory  
Berkeley, CA 94720

Dr. T. Fessenden  
Lawrence Livermore National Laboratory,  
P.O. Box 808  
Livermore, CA 94550

Dr. A. Fisher  
Physics Department  
University of California  
Irvine, CA 92664

Prof. H.H. Fleischmann  
Laboratory for Plasma Studies and  
School of Applied and Engr. Physics  
Cornell University  
Ithaca, NY 14850

Dr. T. Fowler  
Associate Director  
Magnetic Fusion Energy  
Lawrence Livermore National Laboratory,  
P.O. Box 808  
Livermore, CA 94550

Dr. T. Franklin  
EG&G  
Goleta, CA

Dr. T. Genoni  
Air Force Weapons Laboratory  
Kirtland AFB, NM

Dr. B. Godfrey  
Mission Research Corporation  
1400 San Mateo Blvd. S.E.  
Suite A  
Albuquerque, NM 87108

Dr. S. Graybill  
Harry Diamond Laboratory  
2800 Powder Mill Road  
Adelphi, MD 20783

Dr. J.U. Guillory  
JAYCOR  
20550 Whiting St.  
Suite 500  
Alexandria, VA 22304

Dr. Z.G.T. Guiragossian  
TRW Systems and Energy RI/1070  
Advanced Technology Lab  
1 Space Park  
Redondo Beach, CA 90278

Dr. G.P. Gupta  
Scientific Officer  
Bhabha Atomic Reserach Centre  
(MHD Generation Project)  
Bombay, India 400085

Prof. D. Hammer  
Laboratory of Plasma Physics  
Cornell University  
Ithaca, NY 14850

Dr. David Hasti  
Sandia National Laboratory  
Albuquerque, NM 87115

Prof. R. Helleman  
Georgia Institute of Technology  
Atlanta, Georgia 30332

Dr. Ross Hester  
Lawrence Livermore National Laboratory,  
P.O. Box 800  
Livermore, CA 94550

Dr. C.E. Hollandsworth  
Ballistic Research Laboratory  
DRDAB - BLB  
Aberdeen Proving Ground, MD 21005

Dr. S. Humphries  
Sandia Laboratories  
Albuquerque, NM 87115

Dr. Robert Hunter  
Western Research Inc.,  
San Diego, CA

Dr. J. Hyman  
Hughes Research Laboratory  
3011 Malibu Canyon Road  
Malibu, CA 90265

Prof. H. Ishizuka  
Department of Physics  
University of California at Irvine  
Irvine, CA 92664

Prof. K. Karoumbalos  
Department of Physics  
University of Athens  
Athens, Greece

Dr. Takaya Kawabe  
Institute of Plasma Physics  
Nagoya University  
Nagoya 464  
Japan

Dr. Shigeo Kawata  
Tokyo Institute of Technology  
Tokyo, JAPAN

Dr. D. Keefe  
Lawrence Berkeley Laboratory  
Berkeley, CA 94720

Dr. Donald Kerst  
University of Wisconsin  
Madison, WI

Dr. J.D. Kilkenny  
Department of Physics  
Imperial College  
Prince Consort Road  
ENGLAND

Dr. Edward Knapp  
Los Alamos Scientific Laboratory  
Los Alamos, NM

Dr. A. Kolb  
Maxwell Laboratories  
San Diego, CA 92125

Dr. A. Kolomensky  
Lebedev Physical Institute  
Moscow, USSR

Dr. Peter Korn  
Maxwell Laboratories  
San Diego, CA 92125

Dr. D. Lebedev  
Academy of Sciences of USSR  
P.N. Lebedev Physical Institute  
Moscow, Leninsky Prospect, 53 USSR

Dr. R. Linford  
Los Alamos Scientific Laboratory  
P.O. Box 1663  
Los Alamos, NM 87545

Dr. C.S. Liu  
General Atomic Corporation  
La Jolla, CA 92037

Prof. R.V. Lovelace  
School of Applied and Eng. Physics  
Cornell University  
Ithaca, NY 14853

Dr. S.C. Luckhardt  
Plasma Fusion Center  
Mass. Inst. of Technology  
Cambridge, MA 02139

Dr. John Madey  
Physics Department  
Stanford University  
Stanford, CA 94305

Dr. J.E. Maenchen  
Physics International Inc.  
2700 Merced St.  
San Leandro, CA 94577

Dr. A. Mondelli  
c/o Code 4790 Naval Reserach Laboratory  
Washington, DC 20375

Dr. A. Maschke  
Brookhaven National Laboratory  
Upton, L.I. NY

Dr. M. Masuzaki  
Institute of Plasma Physics  
Nagoya University  
Nagoya, Japan

Prof. T. Marshall  
School of Engineering and Applied Science  
Plasma Laboratory  
S.W. Mudd Bldg.  
Columbia University  
New York, NY 10027

Dr. D.A. McArthur  
Sandia National Laboratories  
Albuquerque, NM 87115

Prof. J.E. McCune  
Depart. of Aero. and Astro.  
Mass. Inst. of Technology  
77 Massachusetts Ave.  
Cambridge, MA 02139

Dr. J. McNally, Jr.  
Oak Ridge National Lab.  
P.O. Box Y  
Oak Ridge, TN 37830

Prof. G.H. Miley  
Chairman  
Nuclear Engineering Program  
214 Nuclear Eng. Lab.  
Urbana, IL 61801

Dr. Bruce Miller  
Sandia National Laboratory  
Albuquerque, NM 87115

Prof. A. Mohri  
Institute of Plasma Physics  
Nagoya University  
Nagoya, JAPAN

Dr. Ralph Moir  
L-386  
Lawrence Livermore National Laboratory,  
P.O. Box 808  
Livermore, CA 94550

Dr. Phillip Morton  
Stanford Linear Accelerator Center  
Stanford, CA 94305

Dr. M. Nahemow  
Westinghouse Electric Corporation  
1310 Beulah Rd.  
Pittsburgh, PA 15235

Prof. J. Nation  
Lab. of Plasma Studies  
Cornell University  
Ithaca, NY 14850

Dr. V.K. Neil  
Lawrence Livermore National Laboratory  
P.O. Box 808  
Livermore, CA 94550

Dr. Joan Ogden  
Princeton Plasma Lab.  
Princeton, NJ

Dr. C.L. Olson  
Sandia Laboratory  
Albuquerque, NM 87115

Dr. D. Overskei  
General Atomic Corporation  
La Jolla, CA 92037

Dr. A.S. Paithankar  
Government of India  
Bhabha Atomic Research Centre  
MHD Project  
PRIP SHED  
Trombay  
Bombay 85

Dr. C.A. Patou  
Ctr. D'Etudes Valduc  
B.P. 14  
21120 Is Sur Tillie  
FRANCE

Dr. Arthur Paul  
Lawrence Livermore National Laboratory,  
P.O. Box 808  
Livermore, CA 94550

Dr. S. Penner  
National Bureau of Standards  
Washington, DC 20234

Dr. I.I. Pervushin  
Academy of Sciences of USSR  
Radiotechnical Institute  
8 Marta Str. 10-12  
125083 Moscow A-83, USSR

Dr. Jack M. Peterson  
Lawrence Berkeley Laboratory  
Berkeley, CA 94720

Dr. R. Post  
Lawrence Livermore National Laboratory  
P.O. Box 808  
Livermore, CA 94550

Dr. Kenneth Prestwich  
Sandia National Laboratory  
Albuquerque, NM 87115

Dr. S. Prono  
Lawrence Livermore National Laboratory  
P.O. Box 808  
Livermore, CA 94550

Dr. Sid Putnam  
Pulse Sciences, Inc.  
1615 Broadway  
Suite 700  
Oakland, CA 94612

Dr. Venkat Ramani  
554 Exp'l Plasma Physics  
Phys. Res. Lab.  
Navrangpura Ahmedabad -380-009  
INDIA

Dr. Louis L. Reginato  
Lawrence Livermore National Laboratory  
P.O. Box 808  
Livermore, CA 94550

Prof. N. Reiser  
Dept. of Physics and Astronomy  
University of Maryland  
College Park, MD 20742

Dr. M.E. Rensink  
Lawrence Livermore National Laboratory  
P.O. Box 808  
Livermore, CA 94550

Mr. D. Rej  
Lab for Plasma Physics  
Cornell University  
Ithaca, NY 14853

Dr. J.A. Rome  
Oak Ridge National Laboratory  
Oak Ridge, TN 37850

Prof. Norman Rostoker  
Dept. of Physics  
University of California  
Irvine, CA 92664

Dr. L.I. Rudakov  
I.V. Kurchatov Institute of  
Atomic Energy  
Moscow, USSR

Prof. D. D. Ryutov  
Siberian Branch of Academy of Science  
of USSR  
Institute of Nuclear Physics  
Novosibirsk, USSR

Dr. V.P. Sarantsev  
Jt. Institute for Nuclear Research  
Head Post Office, P.B. 79 Moscow  
Dubna, USSR

Dr. J. Sazama  
Naval Surface Weapons Center  
Code 431  
White Oak Laboratory  
Silver Spring, MD 20910

Prof. Hans Schamel  
463 Bochum -  
RUHR-Universitat  
W. Germany

Prof. George Schmidt  
Physics Department  
Stevens Institute of Technology  
Hoboken, NJ 07030

Prof. P. Seraphim  
Electrical Engineering Department  
National Technical University of Athens  
Athens, Greece

Dr. Andrew Sessler  
Lawrence Berkeley National Laboratory  
Berkeley, CA 94720

Dr. Ian Smith  
Pulse Sciences Inc.  
Oakland, CA

Dr. Lloyd Smith  
Lawrence Berkeley National Laboratory  
Berkeley, CA 94720

Dr. A. Sternlieb  
Lawrence Berkeley National Laboratory  
Berkeley, CA 94720

Dr. D. Straw  
Air Force Weapons Lab  
Kirtland AFB, NM 87117

Prof. C. Striffler  
Dept. of Electrical Engineering  
University of Maryland  
College Park, MD 20742

Prof. R. Sudan  
Laboratory of Plasma Studies  
Cornell University  
Ithaca, NY 14850

Prof. A.W. Trivelpiece  
Science Applications Inc.  
San Diego, CA 92123

Dr. S.S. Tserevitinov  
Kurchatov's Institute of Atomic Energy  
Moscow, USSR

Dr. W. Tucker  
Sandia National Laboratory  
Albuquerque, NM 87115

Dr. H. Uhm  
Naval Surface Weapons Center  
White Oak Laboratory  
Silver Spring, MD 20910

Prof. R. Uzan  
Laboratoire D'emission Electronique  
Faculte des Sciences  
43, Bd du 11 Novembre 1918  
69 - Villeurbanne, France

Dr. E.S. Weibel  
c/o Center do Recharches  
en Physique de Plasmas  
Ecole Polytechnique Federale  
de Lausanne  
Avenue des Bains 21  
CH-1007, Lausanne, Switzerland

Dr. William Weldon  
University of Texas  
Austin, TX

Dr. Mark Wilson  
National Bureau of Standards  
Washington, DC 20234

Dr. P. Wilson  
Stanford Linear Accelerator Center  
Stanford, CA 94305

Prof. C.B. Wharton  
Occidental Reserach Corp.  
2100 SE Main Street  
Irvine, CA 92713

Dr. Gerald Yonas  
Sandia National Laboratory  
Albuquerque, NM 87115

Defense Technical Information Center - 2 copies

NRL Code 2628 - 20 copies

NRL Code 4700 - 26 copies

NRL Code 4704 - 75 copies

NRL Code 2627 - 20 copies